8-31-2017

Optimization of the Hot Embossing Parameters and Sintering Characterization for Alumina/Berea Sandstone Sintering

Justin F. Robbins
Louisiana State University and Agricultural and Mechanical College

Optimization of the Hot Embossing Parameters and Sintering Characterization for Alumina/Berea Sandstone Sintering

A Thesis

Submitted to the Graduate Facility of the
Louisiana State University and
Agricultural and Mechanical College
In partial fulfillment of the
Requirements for the degree of
Masters' of Science

in

Mechanical Engineering

by
Justin Robbins
B.S.M.E., University of Memphis, 2014
December 2017

Acknowledgements

First and foremost, I would like to thank Dr. Ingmar Schoegl for his guidance and support throughout my graduate career. Without his assistance and advice, this would not have been possible.

Secondly, I would like to acknowledge Dr. Khurshida Sharmin who trained me on the process she developed for the ceramic fabrication and trusted me to continue her work.

I would like to thank my advisory committee: Dr. Schoegl, Dr. Nikitopoulos, and Dr. Guo. Thank you for evaluating my research work and thesis.

I would also like to thank Dr. Nikitopoulos and Dr. Park for their collaboration and input. Dr. Negulescu, thank you for allowing me to use the torque rheometer for batch of the ceramic pastes. I am also thankful for Dr. Guo allowing the use of his furnace for sintering.

Next, I want to thank all of the lab members: James Gigenheimer, Pawan Sharma, Veerendra Naralasetti, Navid Roohani, Girguis Sedkey, Wei Zhao, and Miguel Nabatilan. Special thanks to Wei and Miguel who constructed the RTI imager, took RTI images of samples, and assisted in the batching process. Girguis also assisted with batching. I would also like to thank all the other friends I have made here at LSU in the Mechanical Engineering department.

Finally, thank you to by beautiful wife, April Robbins, and my family for all of the love and support through these last couple of years.

Table of Contents

List of Tables

List of Figures

Abstract

The purpose of this study is to investigate the process of hot embossing on alumina based ceramics as a cost-efficient procedure for manufacturing microfluidic testing components. Alumina ceramics were used as an exploratory phase for the final objective of the project, manufacturing of Berea sandstone based ceramic samples. Previous research has shown potential in using hot embossing on Alumina based ceramics; however, complications with extrusion and micro-structure quality were observed. For this reason, the research performed aimed to produce Berea Sandstone based components by first improving upon the embossing quality of alumina ceramics.

The thesis first investigates changes in the extrusion ratio and the subsequent effects observed on the quality of extrudate. Next, improving the quality of embossed microstructures is examined. This is done by varying the MFI as well as changing the embossing speed and temperature. Finally, a preliminary study into the effectiveness of Berea sandstone based ceramics is reported.

The improved ram extruder demonstrated improved surface quality in post-extrusion samples which can be attributed to a greater extrusion ratio, enhanced temperature uniformity, and changing the extruder stock material to stainless steel. Alumina samples extruded from the new extruder had an average surface roughness of ± 2.03 μm compared to ± 5 μm reported for the previous design.

Comparisons of optical scan data showed that a lower MFI provided sharper edges along the testing section; however, demolding from the embossing plate was a challenge often rendering samples unusable. The higher MFI was very easy to demold from the embossing plate and the resolution of the imprinted microstructures improved; therefore, the higher MFI was chosen and

other embossing parameters were examined: embossing temperature and speed. It was concluded that low viscosity and slow embossing speeds provide higher quality embossed samples.

After inspection of several embossing parameters on microstructure quality, an introductory study into Berea sandstone ceramics was conducted. During sintering, a properly densified sample was not obtained and SEM results indicated a loss of iron oxide on the periphery of the sample. However, this initial step in manufacturing sandstone samples provides invaluable insight into the future of the project.

Chapter 1
Introduction

1.1 Motivation and Problem Statement

Microfluidics is the study of movement, handling, and manipulations of liquid in sub-millimeter scale structures [1]. This area of fluid transport has implications in several other fields of study: oil and gas recovery, water purification, DNA sequencing, combustion, carbon sequestration, and information technology [2] [3] [4] [5] [6]. However, many current analyzing techniques require expensive equipment and flow fields cannot be easily visualized. Therefore, this study manufactures a ceramic microfluidic chip by hot-embossing microstructures onto the sample and sealing these channels using a transparent material, borosilicate glass. This allows for optical analysis of flow fields resulting in a higher level of understanding and cost-efficient analyses.

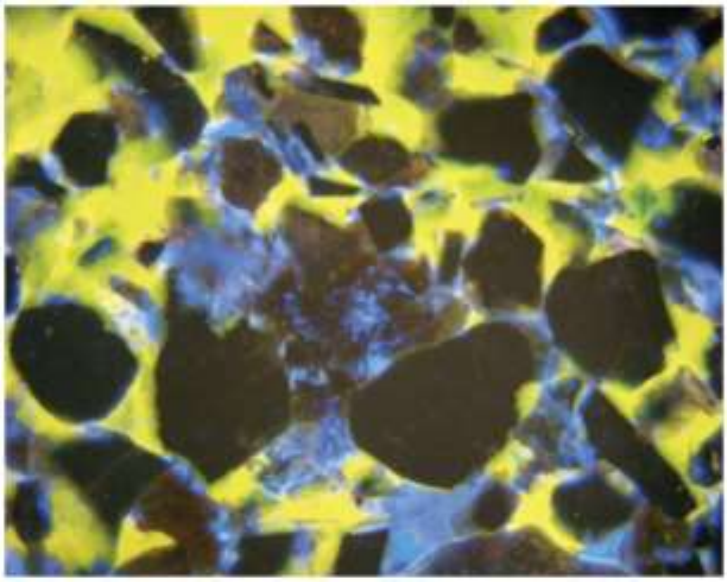

Figure 1: Thin cross-section of oil-bearing sandstone showing oil (blue) and water (yellow) occupying the space between the grains of the Sandstone [7].

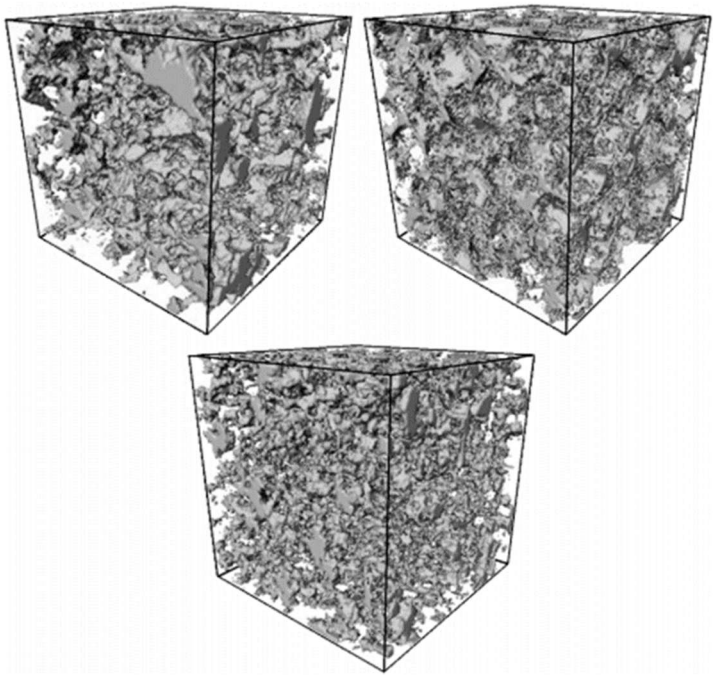

Figure 2: A 1283 voxel 3D image demonstrating the porosity of Berea Sandstone [8].

Berea sandstone is one of the most frequent geological formations surrounding water, oil, and natural gas reservoirs in the North-East United States [4]. Figure 1 shows a cross-section of water/oil bearing sandstone material. Therefore, Berea sandstone was chosen as the target ceramic base material for this study. Advantages of using Berea Sandstone as the base of the ceramic are accurately matched material specifications such as chemistry, permeability, porosity, and wettability.

There are two types of sub-surface oil, gas, and water traps: structural traps and stratigraphic traps. Structural traps store fluid in deformed parts of the earth's crust; Stratigraphic traps store fluid inside the pores sandstones and limestones surrounded by an impermeable wall of shale [9]. Most of the remaining oil in the world is likely held in stratigraphic traps [10]. As a result, many studies have been performed that focus on the microfluidics of sandstones to aid in the extraction process.

It is agreed upon in the oil industry that only 20% to 40% of the available oil in a reservoir is captured [1] [7]. Due to high capillary forces found in the pores of sandstones, oil becomes immobile inside the pore structures [7]. Figure 2 illustrates the complex network of pores found within Berea sandstone. With the demand of oil and gas on the rise, improvements to existing recovery enhancement processes need to be developed to further aid well extractions [11]; hydraulic fracturing, or "fracking", and water flooding are examples of some oil recovery enhancement processes [1] [12]. In order to cost-effectively study fluid transport in underground systems, a simulation of real rock porous structures needs to be created which can be analyzed using non-invasive techniques.

1.2 Goals and Approach

The main focus of this stage in the project is to characterize optimal hot-embossing parameters as well as investigate the post-processing techniques proposed by Sharmin on real rock ceramic samples [13]. Hot embossing was performed by heating a combination of a thermoplastic binder (poly-ethylene-co-vinyl acetate) and a precursor powder (Alumina/Berea) to its melting range and imprinting microstructures through compressing the ceramic sample between a metal mold and a flat aluminum disc. Research performed by Sharmin showed promise in using Alumina based ceramics with hot embossed microstructures, but extrudate surface quality, demolding issues, and optimal hot embossing parameters needed to be investigated. The aim of this stage is to expand upon this research by redesigning the ceramic extruder and enhancing both demolding condition and microstructure resolution by changing the ceramic formulation or embossing parameters.

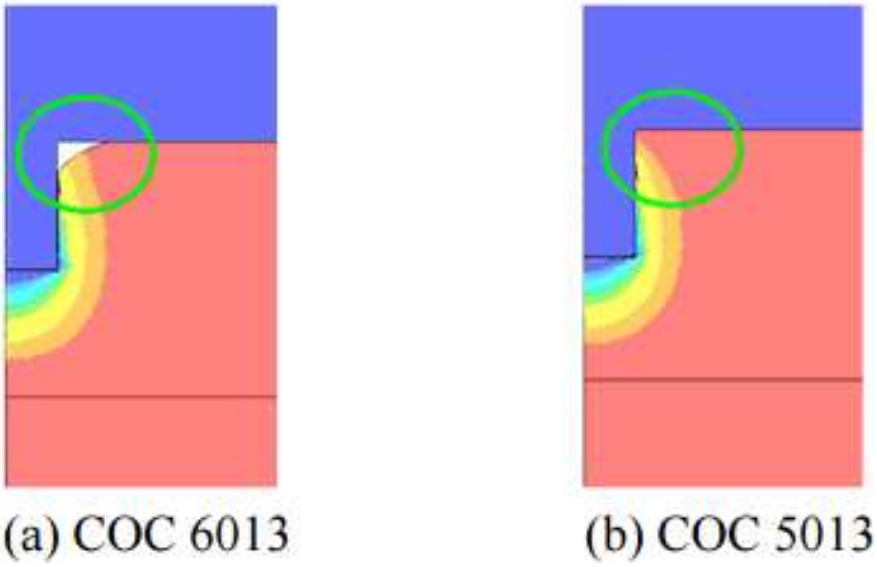

Figure 3: FE simulation illustrating cavity filling for low MFI (a) compared to high MFI (b) [14].

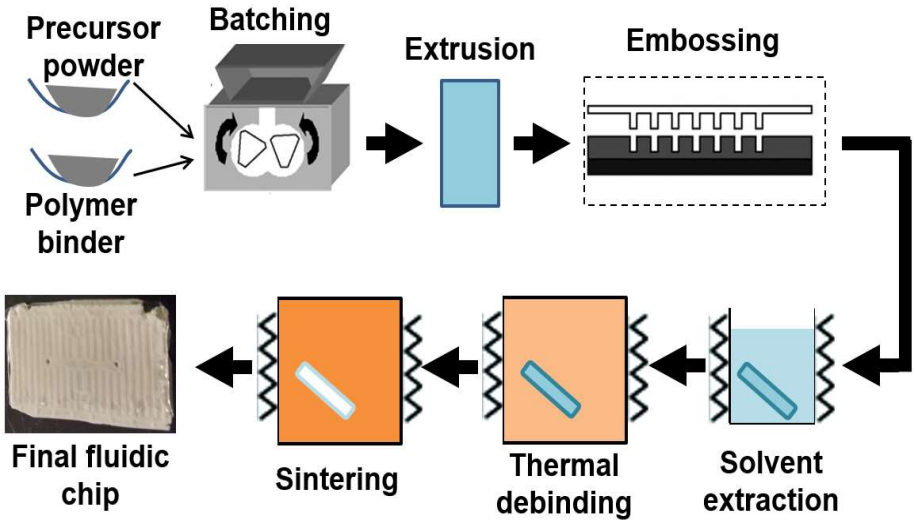

Figure 4: Graphics explaining the extrusion and embossing technique mentioned [13].

A custom-built ram extruder was manufactured for the shaping of ceramic agglomerates. A ram extruder is an extruder which uses a piston to push material through a die to form a desired geometry. The new extruder allowed for an analysis of how the extrusion ratio and temperature uniformity in the die effect the quality of ceramic extrudate.

Quality of embossed microstructures was tested by changing the rheology of the ceramic components as well as changing embossing parameters: embossing speed, temperature, and cooling rate. The rheology of the ceramic paste was varied by changing the melt flow index (MFI) of the thermoplastic binder, poly-ethylene-co-vinyl-acetate (EVA). A study performed by Sahli, et. al. indicates that the rate of filling for hot embossed microstructures increases with increased MFI resulting in higher resolution patterns [14]. Figure 3 demonstrates the effect of the MFI on the filling of microstructures.

After embossing of the ceramic samples, the material needs to be densified to a state where it is completely vitrified. This allows for the flow of fluid through the microchannels without being absorbed by the material. A two-step debinding strategy, solvent extraction and thermal debinding, and finally sintering were used to achieve this goal. The steps are outlined in Figure 4.

1.3 Outline

Chapter 2 is the literature review. First, a look into common microfluidic approaches is presented. Then, research into micromodel fabrication done by Sharmin is cited. Ram extruder design and defects formed during the process are explored next. Finally, an investigation into the sintering of silica/quartz based ceramics is given.

Chapter 3 reviews the materials used; this includes the formulation for Alumina and Berea sandstone ceramics. This chapter also presents the methods used to obtain a densified ceramic micro-model.

Chapter 4 is the results section. This chapter starts off by comparing the effects of the newly designed ram extruder to the previously used version. Next, a look into optimizing the hot

embossing process is investigated. Finally, sintering of Berea sandstone based ceramic material is explored.

Chapter 5 presents the concluding remarks for the project along with future recommendations. Future work includes obtaining fully densified real rock samples.

Chapter 2
Literature Review

2.1 Existing Microfluidic Analysis Approaches

Environmental and economical motivations are what drive research into the study of fluid flow through porous media. There are many existing approaches to analyzing microfluidics; electrokinetics, micromodel simulations, and numerical solutions for example [15] [16] [17] [18] [19]. Electrokinetic analyses are performed by recording the streaming potential induced by the motion of ions in fluid through a porous material [18] [19]. Micromodel simulations of porous rock have previously been performed by etching pores and throats onto glass, epoxy resins, and silicon wafers [16] [15] [17]. Numerical solutions, namely Monte Carlo solutions, are used frequently to predict flow in complex geometries [17]. However, these techniques can be found lacking in either the ability to visualize fluid flows or in chemical composition.

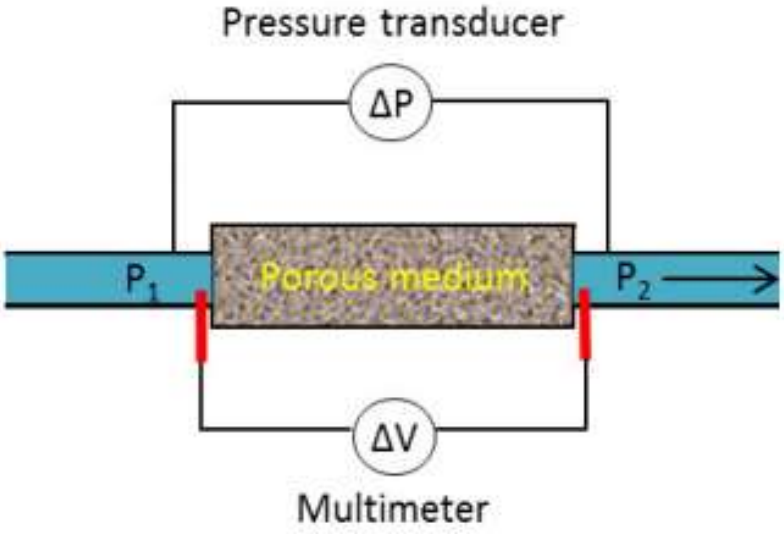

Figure 5: Schematic illustrating the measurement of the streaming potential for electrokinetic analysis [19].

In order to analyze electrokinetic flow, the streaming potential of the flow is investigated. Streaming potential is the electrical current induced by pressure driven flow of electrolytes through a capillary [20]. Theory relating the streaming potential to the pressure drop associated with capillary flow is well defined [21]. Figure 5 shows an illustration of a common approach to measuring the streaming potential in a pressure driven flow. The equation relating the potential to the pressure drop is,

$$C_s = \frac{\Delta V}{\Delta P} = \frac{\varepsilon_r \varepsilon_0 \zeta}{\eta \sigma_{eff}} \quad (1)$$

where ΔV is the streaming potential, ΔP is the fluid pressure drop, ε_r is the electric permittivity of the fluid, ε_o is the dielectric permittivity in vacuum, η is the dynamic viscosity of the fluid, σ_{eff} is the effective conductivity, and ζ is the zeta potential [19]. Results from Moore et. al. on liquid carbon sequestration techniques suggest that the amount of trapped/bound water in sandstones has a direct effect in its electrokinetic response.

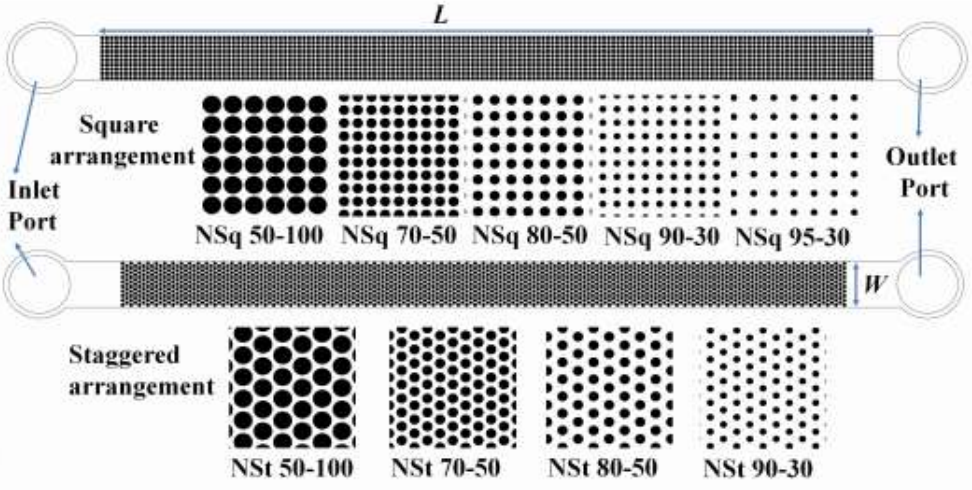

Figure 6: Typical geometries used in structured media to visualize flow through porous media [17].

Micromodel simulations, structured geometrical patterns etched into glass, epoxy, or resin, have been used extensively for porous flow analyses. Figure 6 shows a common approach to

simulating porous structures by using an array of pillars. A study performed by Campbell et. al. examined how crude oil and refined oil are displaced by CO_2/water flooding in porous networks. This was completed by etching a simulation of a porous 2D network onto glass plates [16]. Research conducted by Chen et. al. explored systems of porous networks by etching pores, connected by throats, onto a transparent epoxy. This study investigated the displacement of fluid using one and two-phased flows [15]. Etching of silicon wafers as a process of simulating porous rock was performed by Joseph [17]. While the first two studies explored overall flow patterns of capillary flow, Joseph looked into characterizing transport properties, such as porosity and permeability, in structured and unstructured porous media [17]. Structured porous media is characterized by ideal geometries such as cylindrical pillars arranged in a square pattern [15] [16] [17]. This is important in analyzing components such as heat exchangers. Unstructured media investigated by Joseph was obtained by looking into real rock networks and etched onto a silicon wafer [17]. This was done to create a more realistic porous network for visualization of flows in inherently unstructured media such as Berea Sandstone [17]. Campbell et. al. and Chen et. al. both reported that their pore simulations were not accurate representations of real porous structures. This study aims to alleviate many of the sources of error proposed by Campbell, Chen, and Joseph by creating a pseudo-3D (2.5D) geometry and by matching the wettability of real rock by using Berea Sandstone at the base material in the embossed ceramic component.

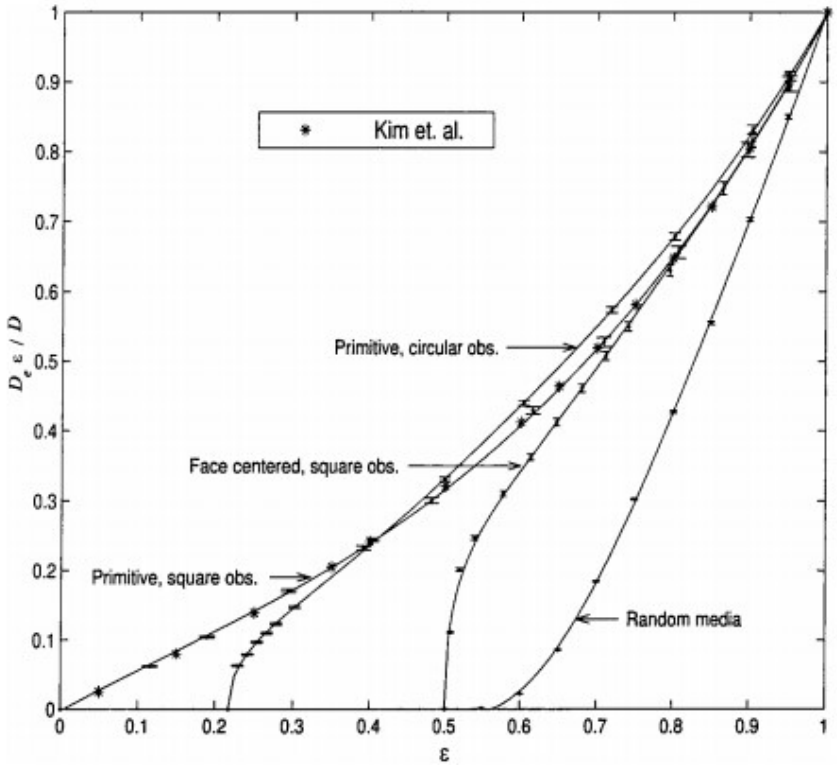

Figure 7: Effective diffusivity found using the Monte Carlo method to investigate 2D media [22].

When studying complex geometries, numerical solutions are often implemented to predict solutions. The Monte Carlo method provides an approach of converging to a solution using generations of random numbers while using a speculative and probabilistic approach [17] [22]. A study performed by Trinh et. al. uses the Monte Carlo method to compare structured media to unstructured media. It was reported that traditional 2D simulations of porosity using structured media is not a good representation of real 3D porous structures [22]. Trinh et. al. attributed this error to a percolation threshold. The percolation threshold is the resulting diminished diffusivity found when a diffusing particle is trapped in an isolated pore [22]. Figure 7 displays the effective diffusivity of structured media compared to unstructured media (random media).

2.2 Microfabrication of Extruded Ceramic-filled Polymer Blends

This project is a continuation of the study performed by the author's predecessor, Sharmin. The objective of Sharmin's study was to create a process for the fabrication of ceramic microstructures. The research approach was to assess the implementation of a two-step debinding process on defects commonly found in the binder removal and sintering stages, by varying the binders, rheological behavior of the material, heating schedule, and microstructures [13].

Ceramic micromodels were created by first compounding the precursor powder, Alumina, with two thermoplastic binders, poly-ethylene-glycol (PEG) and poly-ethylene-co-vinyl acetate (EVA) or polyethylene butyl acrylate (PEBA). After the ceramic paste is created, it is processed through an extruder to create the desired geometry. Next, microstructures are imprinted on the sample via hot embossing. The two-step debinding strategy mentioned earlier is then used to remove the binders from the ceramic before being sintered. Finally the sample capped with a glass slide to create a closed system.

The two-step debinding process was proposed by Thomas-Vielma et. al., Xianfeng et. al., and validated by Sharmin. The process consists of compounding both water soluble binders and traditional thermoplastic binders, such as EVA or PEBA [13]. Removal of the soluble binder creates a larger porous network to in the sample; this allows the pyrolysis products from the decomposition of the thermoplastic binder to escape without damaging the sample [23] [24]. It has been determined that this approach helps to eliminate many defects seen in the PIM post-processing treatment [13] [24] [23].

Figure 8: Edge tearing of ceramic tapes during extrusion [13].

It was recommended by Sharmin to redesign the ram extruder. Extrusion proved challenging as the extrudate exhibited tears along the edges and surface distortions, showing in Figure 8. Edge tearing is indicative of a non-sufficient extrusion ratio [25]. Also, adherence of the glass slides to the ceramic for capping was incomplete. A change in the heating schedule for capping was suggested. The next stage of the project is to investigate the optimal approach for obtaining high resolution microstructures and to begin studies into manufacturing real rock microfluidic chips.

2.3 Ram Extruder Die Design

The batched ceramic agglomerates were shaped to the desired geometry for embossing via ram extruder. The extruder consists of a piston, a reservoir section where the ceramic paste is

loaded and compacted, and a converging, rectangular die. Figure 9 shows the arrangement in detail.

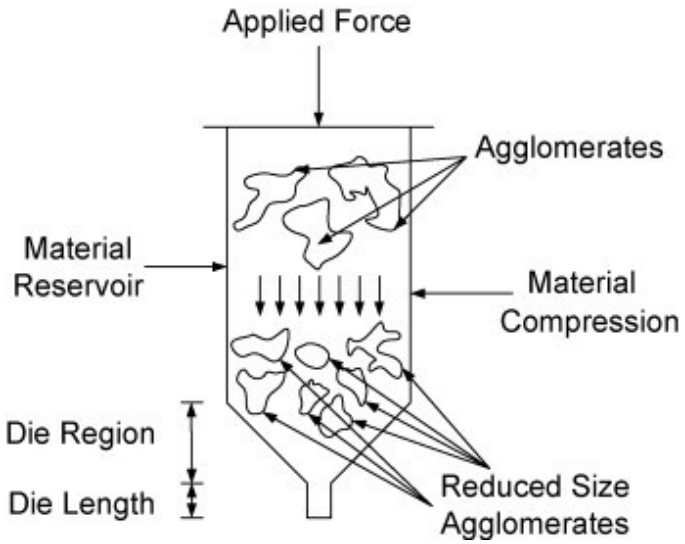

Figure 9: Schematic of a ram extruder [26].

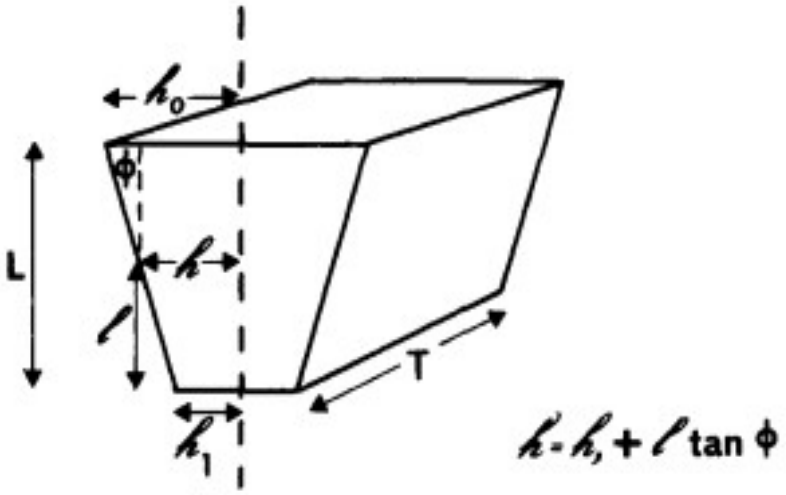

Figure 10: Geometrical parameters of a converging ram extruder die [27].

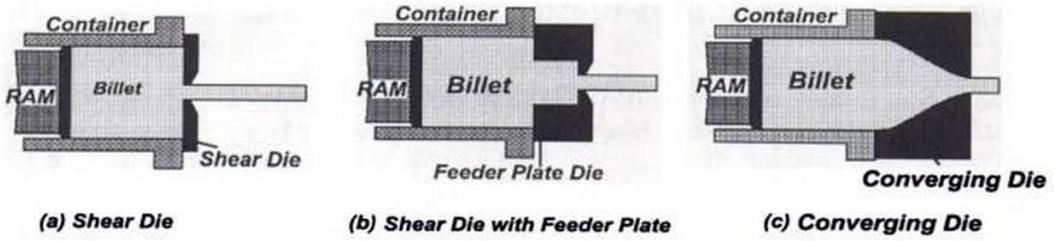

Figure 11: Comparison of conventional shear die designs compared to a converging die design [28].

According to research by Cogswell, the optimal die will maximize output of low surface roughness extrudate as well as minimizing pressure drop and swell ratio [27]. The swell ratio is the ratio of the extruder diameter at the die exit to the actual extrudate diameter [29]. Assuming that shear stress is the dominating stress, the pressure drop of a converging rectangular die and the swell ratio after extrusion can be calculated using:

$$B_{s1}^2 = \frac{2}{3}\gamma_R \left\{ \left(1 + \frac{1}{\gamma_R^2}\right)^{\frac{3}{2}} - \frac{1}{\gamma_R^3} \right\} \quad (2)$$

$$P_s = \frac{\sigma_{s1}}{2n\,tan} \left[1 - \left(\frac{h_1}{h_0}\right)^{2n} \right] \quad (3)$$

where B is the swelling ratio, P is the pressure drop, γ is the recoverable shear strain based on the die exit shear stress σ_{s1}, n is an empirical constant, and φ, h_0, and h_1 are geometrical parameters of the die presented in Figure 10 [27]. Figure 11 compares the geometries of a converging die to a conventional shear ram extruder dies. As explained in the next section, defects during extrusion can be attributed to shear stresses in the die region of the extruder [30]. A study by Mehta et. al. concluded that converging dies resulted in lower loads during extrusion as well as decreased stress in the die when compared to traditional shear dies [28]. Therefore it can be implied that converging geometries for dies will result in fewer sample distortions.

2.4 Defects Formed During Extrusion

The extrusion process is of great importance as this is where a majority of deformation occurs [31]. Common defects found in ceramic extrusion include sharkskin, edge tearing, and the formation of air pockets [25] [26] [30] [32]. Sharkskin, small surface tears resulting in the loss of surface gloss, can be attributed to high shear rates in the die section of the extruder [13] [30]. The development of sharkskin can be seen in Figure 12. Edge tearing was mentioned in Section 2.2 and is the result of an insufficient extrusion ratio. Air pockets in samples can be reduced by following proper paste preparation and initial paste compacting before extrusion [26].

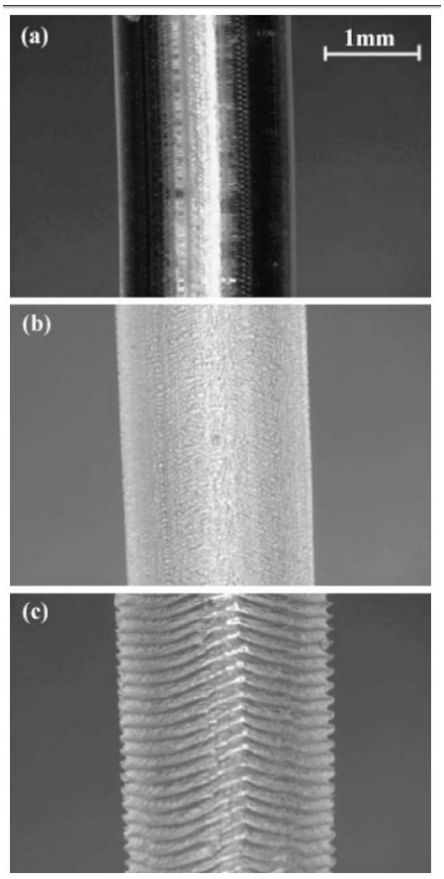

Figure 12: Images showing the transition from smooth (a), to the onset of sharkskin and loss of surface glass (b), and fully developed sharkskin (c) [33].

Most of the defects caused during extrusion can be attributed to high shear stresses at the die exit [26] [27] [30] [32]. Parameters that effect the shear stresses include the rate of convergence of the die, the extrusion ratio, ceramic rheology, and temperature uniformity [34] [35].

The extrusion ratio is the comparison between the initial diameter of the die section to the die exit diameter [26]. Analogous to ceramic extrusion, research in the extrusion of metal powders shows that low extrusion ratio values result in weak bonding between the powder molecules and the material matrix resulting in low quality extrudate; high values resulted in surface deformations due to increased shear rates [35]. For softer aluminum alloys, a normal extrusion range is from 10:1 to 100:1 [36].

2.5 Sintering of Silica Based Ceramics

Berea Sandstone, the objective material of this project, is greater than 90% silica ($Si0_2$) combined with clay, alumina, and numerous feldspar compounds [37]. While sandstone sintering is not well documented, insight into the sintering mechanics of sandstone can be achieved through looking at various silica/quartz concentrated materials such as porcelain stoneware, fired brick, and fused silica ceramics. Porcelain stoneware closely resembles the felsic (combination of feldspar and silica) composition of Berea sandstone but has slightly less of a silica concentration. Two types of fired brick, traditional clay fired and quartz sand bricks, were chosen as to compare how increased silica concentrations impacts sintering mechanisms. Fused silica is a non-crystalline silica material formed by the combustion of silicon containing gases. This allows for the manufacturing of extremely high purity compounds. This section will explore the sintering processes and the mechanics behind the densification of these materials.

2.5.1 Porcelain Stoneware

Porcelain stoneware is described by ASTM C373 as a ceramic tile with a water absorption of 0.5% or less [38]. Commercial porcelain stoneware has a composition of 30-40% clay, 40-50% feldspar, and 10-15% quartz giving it approximately 70%wt. of silica [39] [40] [41]. Porcelain stoneware tiles are sintered using a single fast firing technique, with a cold-to-cold time of 60-90 minutes [39] [40] [41]. This is performed using high heating rates, 50-80 ˚C/min, with a low soak time at the maximum temperature, between 1200-1400˚C [39] [40] [41]. This results in a glassy phase matrix with embedded crystalline phases of mullite, a crystal formed from feldspar reactions as well as the decomposition of pure clays, and residual quartz and feldspar [41] [42].

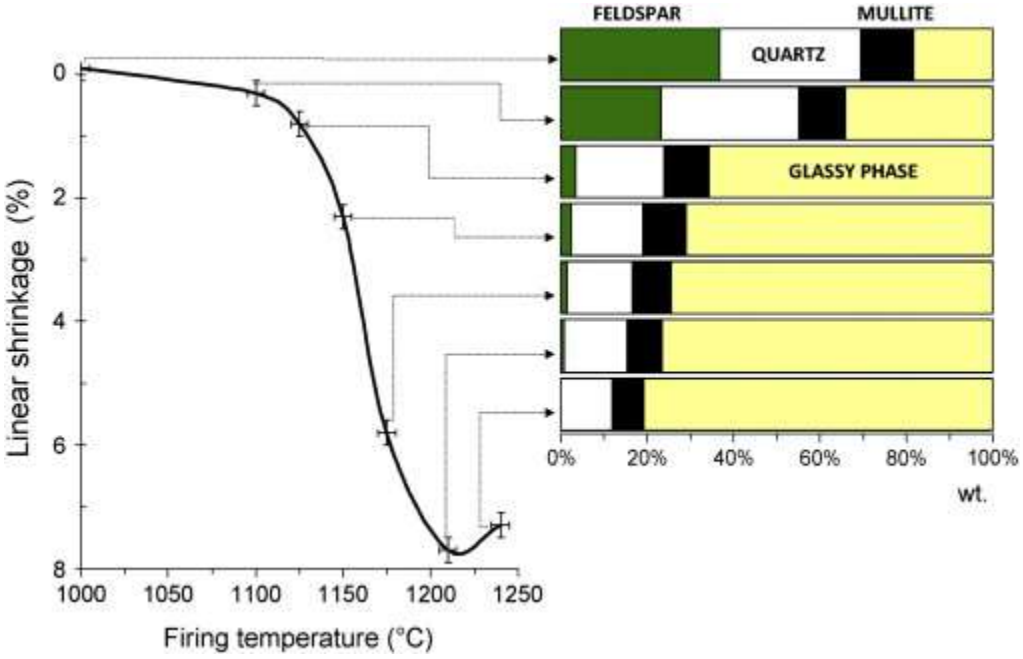

Figure 13: Effect of firing temperature on linear shrinkage and porcelain composition [41].

Research by Zanelli et. al. observed the sintering mechanisms responsible for the sintering of porcelain stoneware by firing the ceramic to a certain temperature range, quenching the sample, and analyzing the initial, intermediate, and final stages of sintering [40]. In the initial stage, 900-1000 ˚C, the main sintering mechanism was found to be surface diffusion, during which clay

minerals decomposed into amorphous phases and the formation of mullite began to occur [40]. Temperature ranges from 1100-1200˚C was considered the intermediate stage. As the temperature increased, the dissolution of quartz into the liquid phase and the amount of feldspar melts increased [40]. Liquid phase melts occur very quickly at this temperature, 60-69% of quartz and feldspar eutectics melt within 5 min., and results suggest that densification at this stage primarily depends on the viscosity of these melts [40] [41]. The final stage overlaps the intermediate stage and is characterized by temperatures exceeding 1175˚C. In this stage, the phase composition reaches an equilibrium state and the only observable change in composition is the further dissolution of quartz along with an increased formation of mullite in the liquid phase [40]. After maximum densification occurs, around 1220˚C, the coarsening of closed pores was observed leading to a decrease in the linear shrinkage of the material as shown in Figure 13 [41]. This was also observed for prolonged hold times at the maximum sintering temperature [40]. Further increase in the temperature lead to swelling and distortions in the porcelain samples [40]. This was analyzed by Martin-Marquez et. al. and attributed to the expelling of trapped gases with in the sample resulting in blisters and bloating [39].

2.5.2 Fired Brick Sintering

Red brick, such as those used as walling material for buildings, are formed by heat treating clay to form a strong, water impervious structure. The chemical composition of clay used has major impacts on the compressive strength, permeability, and water absorption due to the amount and types of phase changes as well as feldspar reactions occurring during heating [43]. During heating, many transformations take place such as the crystallization of quartz and the fusing of feldspar into mullite, orthoclase, and aluminosilicate for example [43].

Johari et. al. studied the effect of sintering temperature on the physical performance of clay bricks [43]. This study used clay from a common source in Malaysia which consists of 67%wt. quartz, 26%wt. alumina, along with various feldspar and volatile compounds lost during ignition [43]. The beginning of the sintering process was observed at 900°C when effects of flux components, oxides which reduce the melting temperature of materials such as quartz and alumina, were seen [43]. Solid state sintering was the main process responsible for densification at temperatures between 1000-1100°C [43]. In this range, a 31% reduction in porosity occurred which can be attributed to the growth of grains throughout the sample [43]. At temperatures up to 1200°C, liquid phase sintering took precedence as the melting of quartz and feldspar took place [43]. The liquid phase was able to penetrate the pores of the sample causing a 47.5% decrease in porosity, further increasing the strength of the ceramic.

Recently, studies have begun considering using quartz sands to form bricks due to the abundance of the material and the high consumption of land mass from using traditional clay bricks [44]; Song et. al. studied this substitution [44]. The material used had a higher content of quartz, 84.21%, compared to the clay used in the previously mentioned study [44]. This material is also composed of k-feldspar compounds as well as traces of white mica [44]. It was observed that at 1100°C, the majority of liquid phase in the material was formed from the melting of the k-feldspar, while the increase to 1150°C resulted in the transformation of quartz crystals into the liquid phase [44]. Liquid phases were the focus of this project.

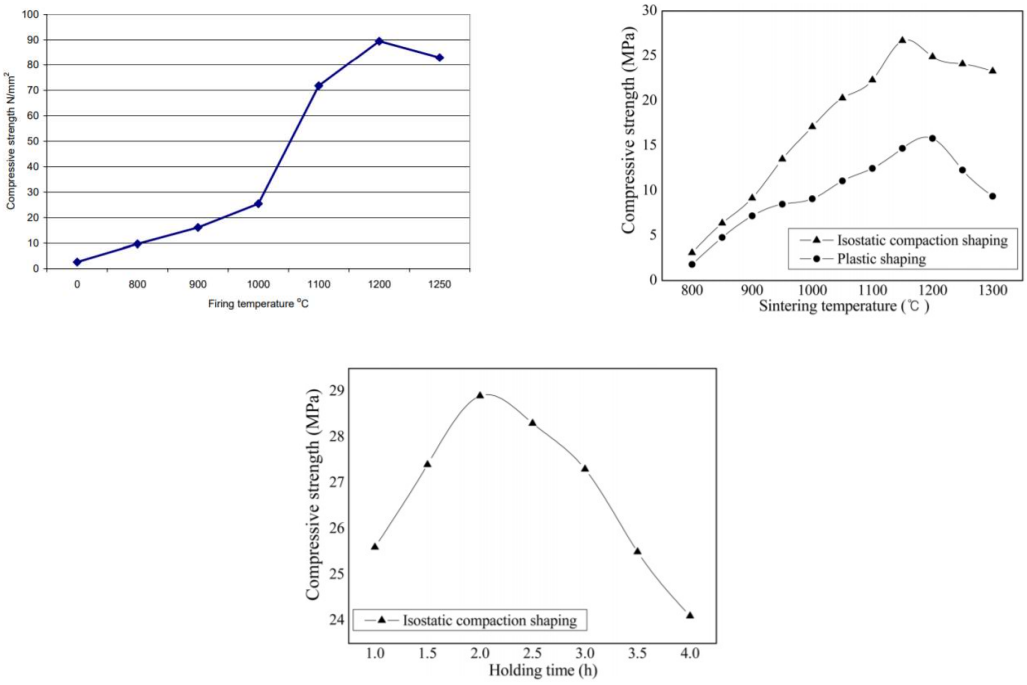

Figure 14: The effect of sintering temperature on clay (a) and quartz (b) bricks. Sintering temperature holding time's impact on quartz bricks (c) [43] [44].

Both Johari et. at. and Song et. al. reported a loss of compressive strength and the formation of open pores when the sintering temperature was increased or for prolonged hold times, shown in Figure 14 [43] [44]. This was attributed to the overabundance of liquid phases causing gas bubbles to be expulsed during over-heating or gas expansion during prolonged sintering times [43] [44].

2.5.3 Sintering of Silica Ceramics

Silica ceramics have many uses ranging from thermal shielding materials for aircrafts to high-temperature microwavable food dishes and wastewater filtering [45] [46]. Many studies focus on fused silica powders as opposed to quartz powders due to its high purity and high transmissions of ultraviolet light [47].

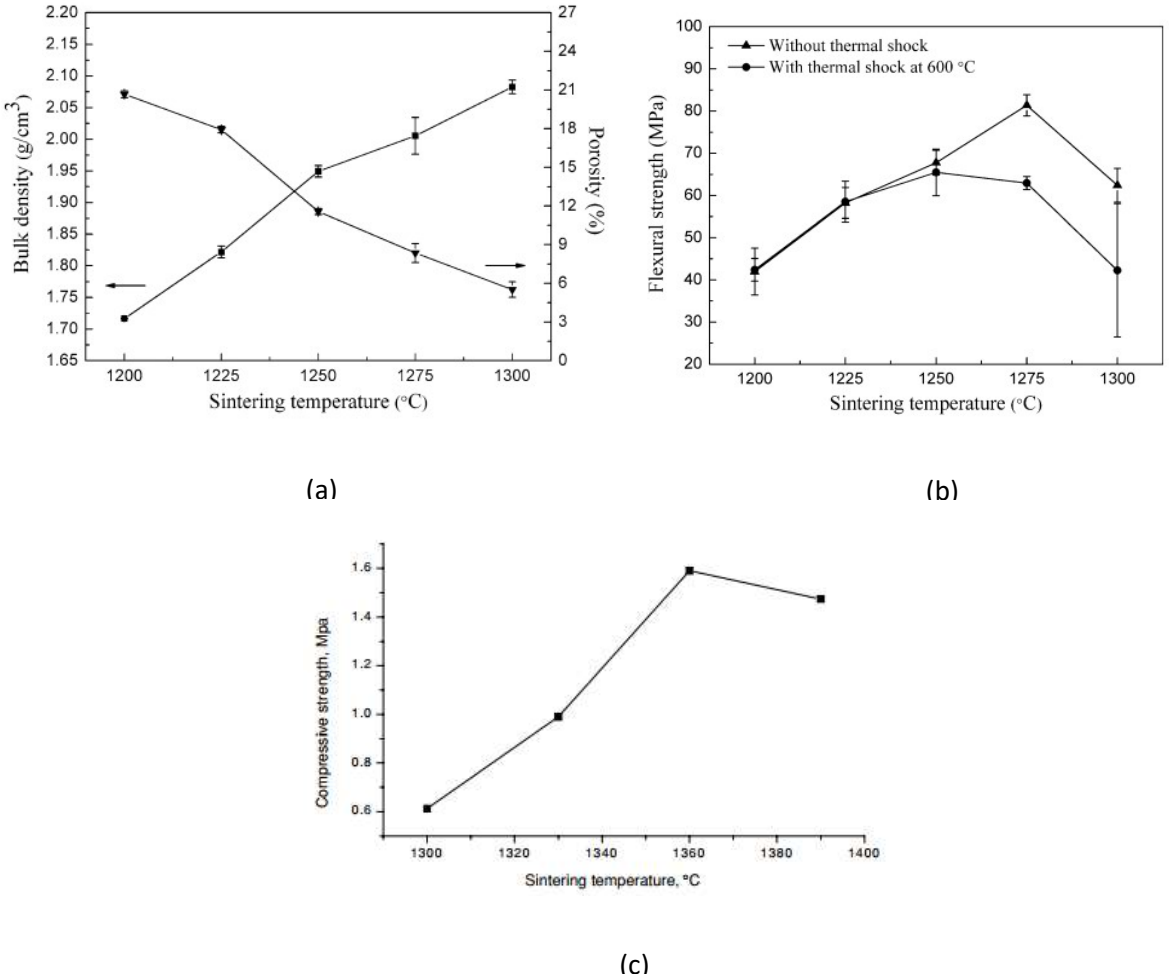

Figure 15: Illustrates the effects of sintering temperature on (a) porosity and bulk density [46], (b) flexural strength [46], and (c) compressive strength [45].

A study conducted by Wan et. al. explores the effect of sintering temperatures on the mechanical and electrical properties of gel casted fused silica ceramics [46]. Heating rates of 5˚C/min or less and a holding time of 4 hours at the maximum sintering temperature, 1200-1300˚C, were used [46]. Decreasing porosity was experienced across the whole temperature range as shown in Figure 15(a), but a decrease in flexural strength occurred at temperatures over 1275°C (Figure 15(b)) [46]. This was due to an increasing amount of silica crystalizing into β-cristobalite [46]. This phenomenon was also reported in a study performed by Han et. al. who was investigating the effects of sintering temperature on the composite strength of porous silica

ceramics; the ceramic in question was created by a mixture of 30%wt clay and 70%wt silica formed into a foam by impregnating a sponge with a silica/clay slurry and compressing the sponge between parallel plates [45]. Figure 15(c) illustrates the effect of the sintering temperature on the compressive strength of the porous silica; the drop in compressive strength was attributed to the formation of cristobalite as well [45].

Wan et. al. also reported cracking occurring during the cooling of ceramics with cristobalite crystals [46]. At low temperatures, between 275-200˚C, cristobalite undergoes a beta-to-alpha transformation changing its structure from a cubic crystal to a tetragonal crystal [48]. This beta-to-alpha transformation was concluded to be the culprit behind crack formations in the fused silica ceramics.

2.5.4 Impact of Pressure and Atmosphere on Quartz/Silica Glass Sintering

As mentioned in the previous section, the quality of sintered silica ceramics is related to the formation of the crystal cristobalite (β-quartz). Research performed by Yong-Taeg et.al. and a patent invented by Orii et. al. explores the use of inert sintering atmospheres and low-pressure sintering as a method to impede the formation of β-quartz.

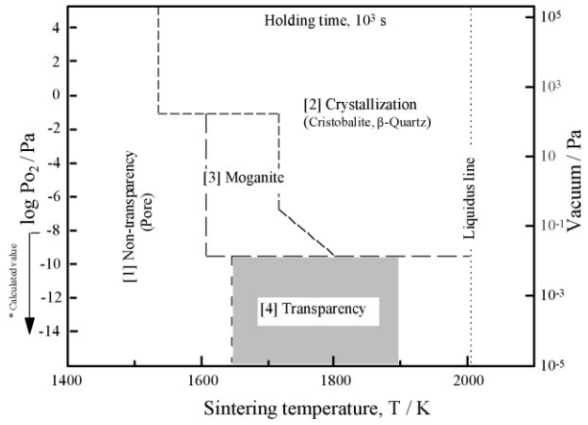

Figure 16: Sintering temperature and pressure effects on crystal formations during sintering [49].

The crystalline phase of sintered silica is directly related to the partial pressure of oxygen in the sintering atmosphere [49]. This is seen in Figure 16 which related the sintering temperature and pressure to the formations of specific crystals. It was recorded that the formation of cristobalite was eliminated in an Argon atmosphere at a pressure of 10 Pa and at 10^{-2} Pa in air [49]. In the argon atmosphere at 10 Pa however, the crystalline phase moganite was formed and at 10^{-2} Pa in air pores were still found in the glass samples [49]. Therefore, a further decrease in the pressure to 10^{-4} Pa was used [49]. This fully eliminated the formation of cristobalite and moganite as well as provided a fully densified sample [49]. Orii et. al. suggests the use of a Helium atmosphere and a pressure of 1.33 Pa [50]. This was found to have minimized the size and amount of pores found within the sintered quartz glass [50]. Both studies recommend the use of a temperature range from approximately 1400-1600˚C [49] [50].

Chapter 3
Materials and Processing Procedures

3.1 Ceramic Paste Composition

Table 1: Relevant properties of the thermoplastic binders used in this study [51] [52].

Thermoplastic Binder (EVA)		
Grade	25-EVA-19	40-EVA-57
MFI (g/10min)	19	57
Melting Point (˚C)	75	75
Acetate % weight	25	40
Density (g/cm$_3$)	0.941	0.941

Table 2: Percent volume compositions of the ceramic pastes.

	Alumina (%vol.)	**Berea Sandstone (%vol.)**
Precursor Powder (Al_2O_3;Berea)	55.25	55.60
Thermoplastic Binder (EVA)	22.69	20.58
PEG 6000	18.56	19.03
PEG 200	3.49	4.77

Table 3: Composition of the Berea precursor powder from EDAX analysis.

Constituent	**Berea Precursor Powder (%)**
Total clay	0.76
Quartz	98.75
K-feldspar	0.19
Plagioclase	0.20

Table 4: Typical Berea Sandstone Mineral Concentrations [53].

Constituent	Berea Sandstone (%)
Quartz	93.13
Alumina	3.86
Ferric Oxide	0.11
Ferrous Oxide	0.54
Magnesium Oxide	0.25
Calcium Oxide	0.10
Loss on Ignition	1.43

The ceramic paste used in this study consists of two types of components, a precursor powder and binding agents [13]. Two precursor powders used in this study: alpha phase alumina and Berea sandstone. Binding agents consist of a water-soluble binder and a thermoplastic backbone binder. Table 1 presents the properties of the thermoplastic binder. Table 2 gives the composition of the ceramics paste. For a more detailed investigation into the materials used, please refer to the author's predecessor's dissertation Sharmin [13].

Alumina ceramics are used in many applications ranging from hip implants to cutting tools [54]. As well as being a cost-effective precursor, alumina is widely used due to its high hardness and favorable thermal properties [13] [54] [55]. This project uses 99.85% purity alpha phase alumina powders with an average particle size of 150 nm and a density of 3.97 g/cm^3 from Inframat Advanced Materials [56].

Many water, oil, and natural gas reservoirs in the northeast are surrounded by Berea sandstone deposits [57] [58]. This is what drives research into the microfluidics of sandstone. While attempts have been made to study flow through porous rock using clear resins and glass, the permeability, porosity, and chemical composition of the real rock is lost. The composition of

the Berea sandstone precursor powder is displayed in Table 3. Table 4 shows the typical mineral concentrations reported from quarries in Cleveland, Ohio. The sandstone used in this study has an average particle size of 1 μm and a density of 2.37 g/cm^3 [59].

The binding components of the ceramic paste consists of two different molecular weights of PEG, PEG6000 and PEG200, and a thermoplastic backbone binder. EVA is used as the backbone binder and helps to maintain the strength of green samples while PEG is used as binder due to its solubility in water. The melting point and density of PEG6000 is 65˚C and 1.21 g/cm^3 respectively [60]. PEG200 is already in the liquid phase and has a density of 1.1 g/cm^3 [61].

3.2 Ceramic Paste Processing

Post-processing of the ceramic paste for alumina ceramics are fully detailed in a paper by Sharmin [13]. Below is a summary of the approach used in this project which follows the author's predecessor's work.

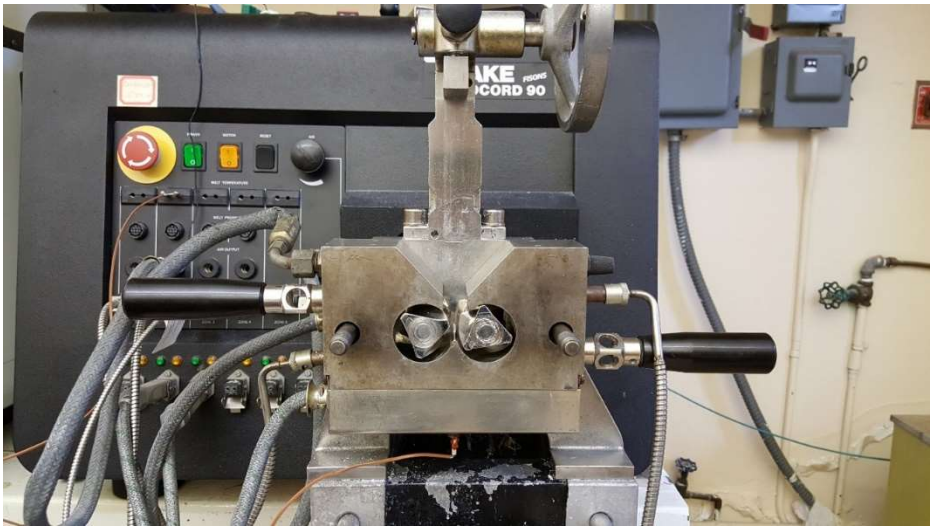

Figure 17: Front view of the Rheocord 90 before the batching process.

3.3 Batch Mixing

Precursor powders and binding components were combined using a HAAKE Rheocord 90. The Rheocord 90 is a twin screw counter-rotating torque rheometer. Twin screw rheometers are

preferred for the batching of ceramics using powders due to the ability of it to disperse fine particles more quickly [62]. Figure 17 shows a front view of the Rheocord 90 before batching ceramic pastes.

For all materials, the batching temperature was set to 110˚C and the screw speed was set to 30 rpm. To ensure proper densification, the solid powder loading was kept at approximately 55% volume [63]. Homogeneity in the paste was qualitatively observed by the stability of torque readings output by the rheometer [62] [63].

The procedure for batch mixing of the ceramics used is as follows. First, the rheometer is allowed to reach the desired temperature before all EVA is added. Once the EVA has become molten, alumina/sandstone is added in small quantities along with a small amount of PEG6000. When the small volume of powder and binder has been fully incorporated, the step is repeated until all powder and PEG6000 has been added. PEG200 is used to control the viscosity of the paste. After all materials are mixed, the paste is removed and mixed again for 5 minutes ensuring homogeneity of the ceramic. Table 2 presents the mixture compositions for alumina and sandstone based samples.

3.4 Extrusion

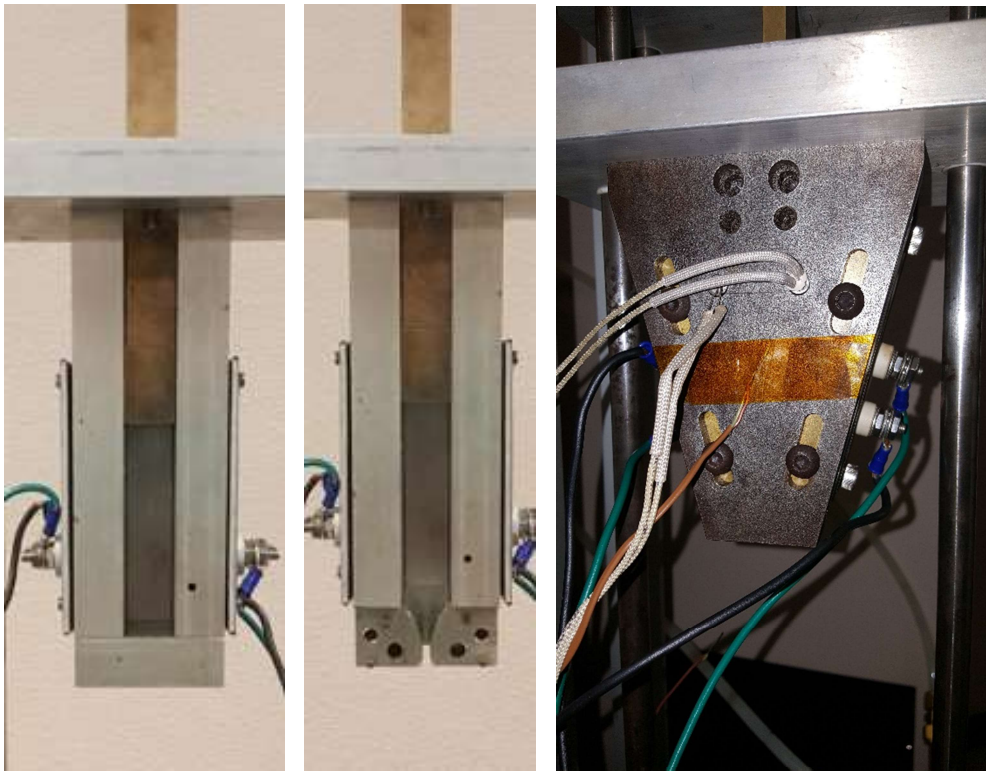

Figure 18: Comparison of new ram extruder with attached packing plate (left) and extrusion die (center) to the old design (right).

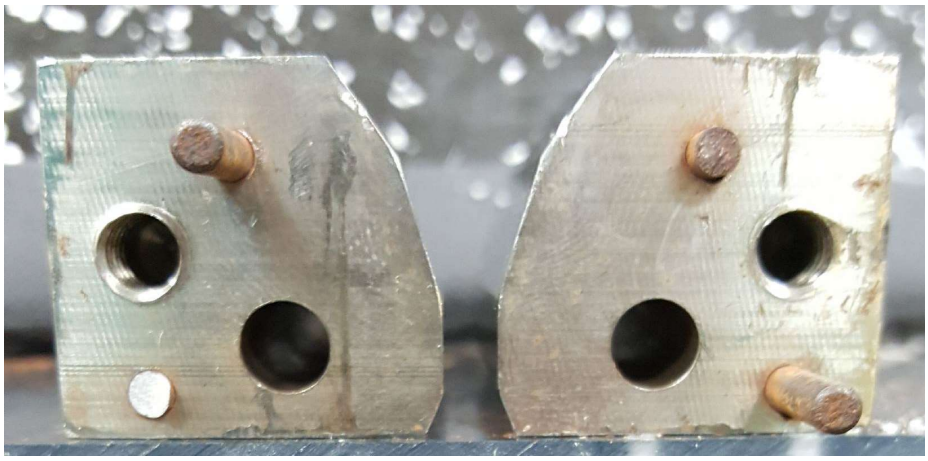

Figure 19: Custom Ram Extruder Dies.

After a batch of ceramic paste is mixed thoroughly, it is processed through a custom ram extruder in order to obtain the desired geometry. The ram extruder is attached to a 30 KN

ComTen Universal Tester (95TL5K) and can be divided into 4 parts: the reservoir section, piston, packing plate, and extrusion die. These can all be seen in Figure 18. The reservoir section is the part of the extruder that holds all the ceramic agglomerates before extrusion. This section is 152.4 mm tall, 50.8 mm wide, and 19 mm thick. A piston is used to compress the material before extrusion and to press the material through the die. The packing plate is used to form the ceramic agglomerates into a continuous structure before extrusion. After initial packing, the ceramic paste is pushed through a custom-made extruder die. Figure 19 shows the geometry of the extruder dies. The first section is a quickly converging section that is 6.35 mm long and has a final extrusion ratio of 2; the second section is a slowly converging section that is 9.53 mm long and has a final extrusion ratio of 6. A relief section is added at the end to lower stresses at the die exit. The die is designed to reduce the amount of shear stress located at the die exit and was also influenced by dimension constraints of the ComTen tester.

Extrusion is performed by letting the extruder, with attached packing plate, heat to 120˚C by using two strip heaters both sides of the reservoir. Temperature is controlled by two thermocouples attached to two Omega CN7500 temperature controllers. Once reached, the ceramic paste is loaded in small intervals and pressed by the piston. This ensures a solid feedstock for extrusion. After all material was loaded, the feedstock was compacted using a pressure of 6.97 MPa. The extruder is allowed to cool so that the packing plate can be replaced by the extruder die. Two cartridge heaters are placed into the walls of the extruder die to supply even heating to the ceramic during extrusion. After being allowed to heat to 120˚C again, the piston pushes the paste through the die. This creates a long tape of ceramics samples which can then be cut to the desired length for embossing.

3.5 Pressing

Before the new ram extruder, shown in the left two pictures of Figure 18, was manufactured an intermediate step between extrusion and embossing was used to ensure consistent thicknesses throughout the sample. The previous extruder, shown in the right-most image of Figure 18, produced ceramic tapes with widely varying thicknesses. The pressing step involves compressing a sample, along with metal spacers to control the final thickness, in-between two aluminum discs. The discs were first sprayed with F-57 Mold Wiz © release agent and placed into a 120˚C oven. Then Carver © heated hydraulic press was heated to a temperature of 120˚C. The sample and spacers were then "sandwiched" between the two aluminum discs and pressed by 1.25 metric tons of force. The pressure was immediately relieved and the system was allowed to cool to room temperature naturally before demolding.

3.6 Embossing

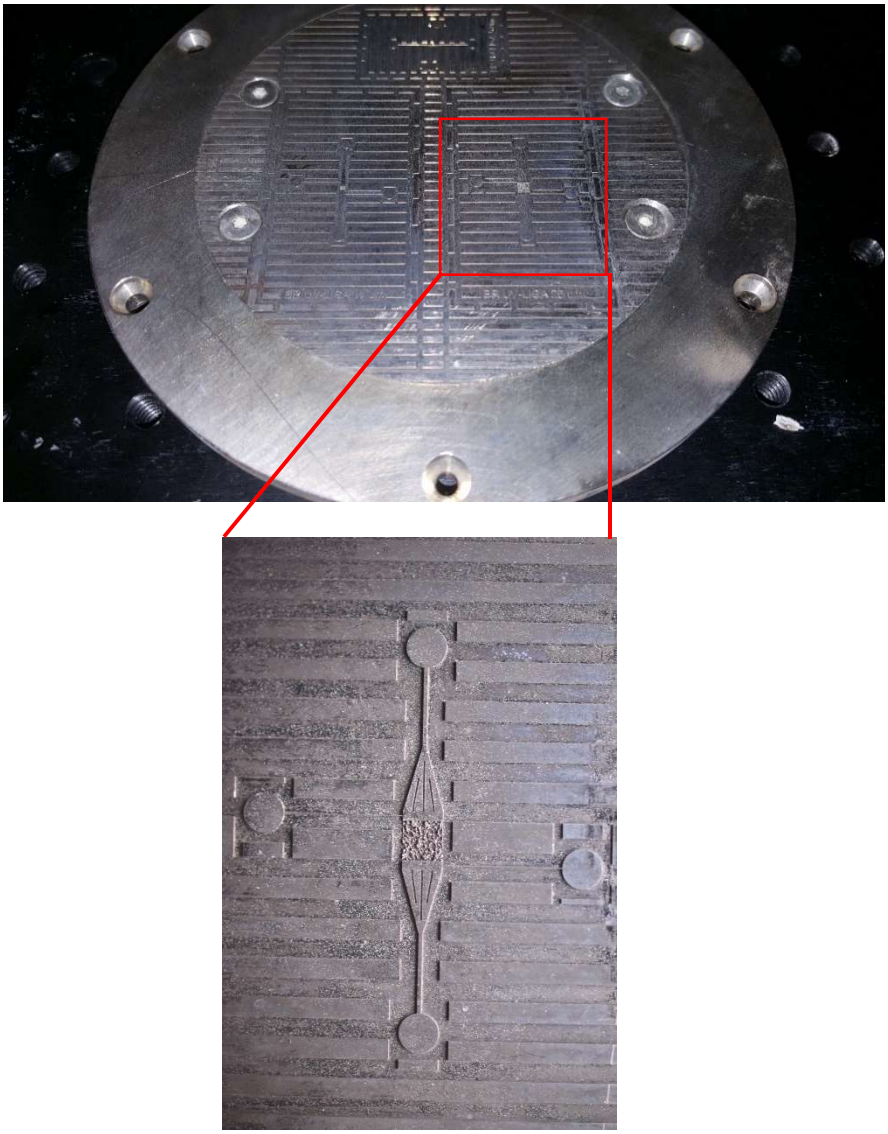

Figure 20: Nickel embossing plate (top) and testing section (bottom).

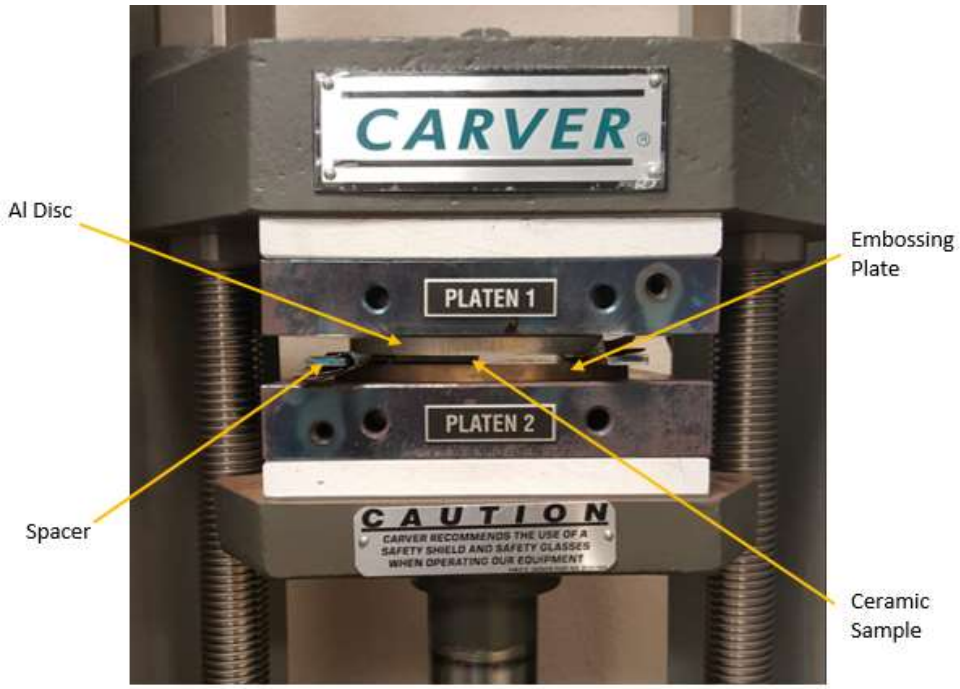

Figure 21: Arrangement of aluminum discs, spacers, sample, and embossing plate in the press.

A Carver © heated hydraulic press is used for embossing [64]. Both the top and bottom platens can be heated and controlled using the same Omega CN7500 temperature controllers used for extrusion. For easy demolding from the aluminum disc and embossing plate, both are coated with an F-57 Mold Wiz © release agent [65].

Embossing was performed by first coating the aluminum disc and embossing plate, Figure 20, with the release agent. They are then put into a 120˚C oven with the ceramic sample. This increases the malleability of the ceramic. The Carver © press is then allowed to heat up to a 120˚C surface temperature. Once all the components are heated, they are arranged on the press as shown in Figure 21. Hydraulic pressure is slowly increased up to 1.25 metric tons then released immediately. The components are then allowed to cool to room temperature before demolding. Next, the samples are processed through several heat treatments described below.

3.7 Two-step Thermal Debinding

Removal of the thermoplastic binder was achieved by a two-step thermal debinding strategy, solvent extraction then thermal debinding. Research by Sharmin validated that this strategy removes many of the defects found during traditional binder removal stages [13].

Initially the water-soluble binder (PEG6000/200) is removed by placing the sample inside a water filled container and left in a 45˚C oven for 4 hours. By removing the water-soluble binder, a larger network of pores is formed. The pores aid in the removal of the thermoplastic binder (EVA) by allowing the gases formed during heating to escape without damaging the sample [13].

The EVA is removed by heating the sample to 1000˚C twice, once in an inert (N_2) atmosphere and once in air. By first allowing the sample to heat in an inert atmosphere, pyrolysis of organic compounds is achieved before removing the carbon residues [13]. The lowered rate of oxidation reactions in the sample helps to prevent crack formations [13].

3.8 Sintering

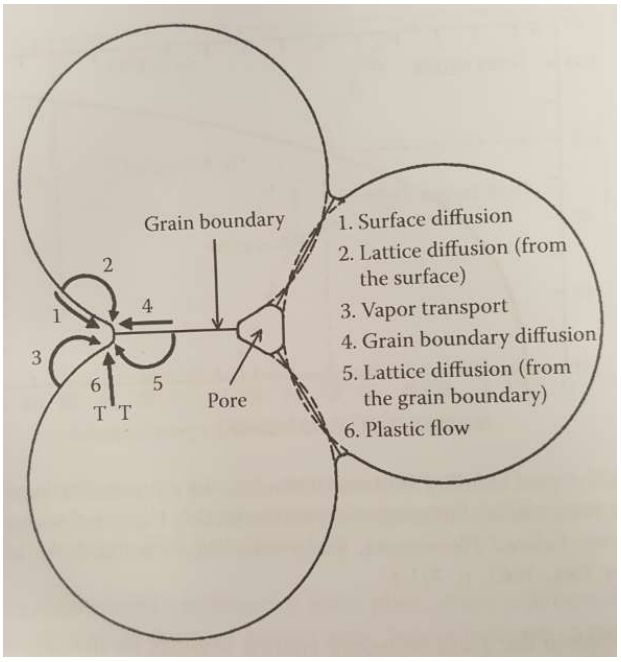

Figure 22: Illustrates the six processes attributed to the sintering of ceramics [66].

After removal of the binding components, the sample must be fired at a sufficiently high temperature in order to attain maximum densification. By lowering the porosity of the sample, water will be able to flow across the microfluidic chip without soaking into the material. This process is called sintering and is achieved through the six steps outlined in Figure 22.

Sintering of ceramic samples was achieved through heating the ceramic between 50% and 80% of the materials melting point. Alumina samples were sintered at 1600˚C for a holding time of 1 hour. Berea samples were sintered at 1232˚C, 1336˚C, and 1450˚C. However, none of the samples densified significantly. This will be discussed in more detail in Chapter 4.

3.9 Capping

Borosilicate glass slides were used to seal the ceramic samples [67]. Following sintering, the glass slide was bonded to the sample through a heating cycle. The glass is brought to its softening point, 720˚C, and held for 1 hour. After bonding, the glass is sent through an annealing phase to relieve any residual stresses. The annealing temperature is 550˚C.

3.10 Characterization Equipment

3.10.1 Scanning Electron Microscope (SEM) and Energy Dispersive Spectroscopy (EDS)

Analyzing densification and chemical composition of Berea sandstone samples were performed with a Quanta 3D FEG SEM with attached EDAX EDS analyzer. For imaging, the samples were coated with platinum by an EMS 550X Sputter coater. This analysis is imperative for understanding the sintering Berea ceramics and to ensure that the chemical composition is preserved throughout all post-processing heat treatments.

3.10.2 Optical Profilometer

Quality of embossed microstructures were quantified using a Nanovea ST400 optical profilometer. The optical profile allows for a side-by-side comparison of microstructure resolution between different samples.

Chapter 4
Results and Discussion

The objective of this study is to validate the optimal process for hot embossing microstructures onto flat ceramic samples. Several factors affecting the outcome of ceramic embossing were investigated including binder MFI, redesign of the ram extruder, changing in demolding spray, embossing speed, embossing temperature, and cooling rate before and after demolding from the embossing plate.

After adequate embossing of alumina ceramics had been accomplished Berea sandstone testing was ready to begin. Chapter 4 will discuss the results obtained from both alumina and Berea sandstone ceramics.

4.1 Extrusion

Before sufficient embossing can be performed, high quality samples must be extruded. Quality ceramic extrudates exhibit low surface roughness and a uniform thickness. These qualities are important during embossing to ensure uniform filling of the embossing plate channels.

Figure 23: Discoloration due to metal corrosion (left) and over-heating (right).

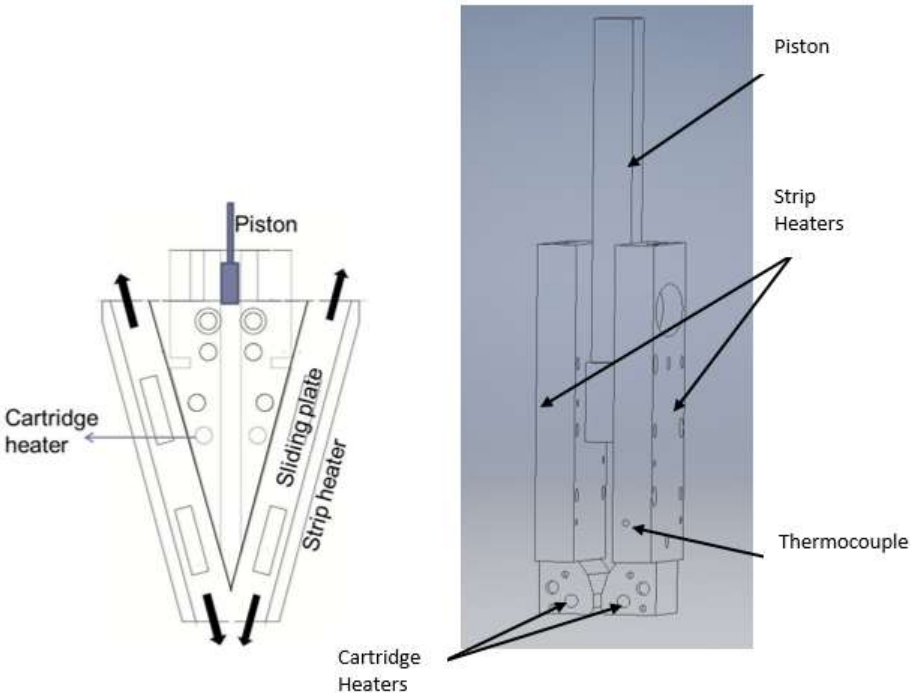

Figure 24: Previous extruder designed by Sharmin (left) [13] and redesigned ram extruder (right).

Table 5: List outlining the pressing parameters changed and the outcome.

Sample Pressing				
Iteration	**MFI (g/10min)**	**Release Agent/Conditions**	**Cooling Environment**	**Observation**
1	19	Endurance© ; sprayed on cold plates	Ambient	Difficult to demold; Loss of material on plates resulting in higher surface roughness
2	19	Endurance© ; sprayed on cold plates	In Press	Very difficult to demold; much higher loss of material left on plates
3	19	Endurance© ; sprayed on cold plates	On Refrigerated Surface	No change from ambient
4	19	Endurance© ; sprayed on preheated plates	Ambient	Less material on plate compared to non-preheated plates, still too rough of a surface
5	57	Endurance© ; sprayed on preheated plates	Ambient	Easier to demold, less material left on plates compared to lower MFI
6	19	Mold Wiz© ; sprayed on preheated plates	Ambient	Less difficult demolding and less material on plates, but still too high of surface roughness
7	57	Mold Wiz© ; sprayed on preheated plates	Ambient	Much easier demolding and small amount of material left on plates
Extruder Redesinged/Pressing Step Eliminated				

During the early stages of the project, an intermediate step between extrusion and embossing was introduced called sample pressing. This step is outlined in Section 3.5. In this phase of the study, the extruder manufactured by Sharmin was used [13]. Extrudate featured a high amount of surface distortions, non-uniform thickness, and discoloration due to over-heating and metal corrosion shown in Figure 23. Difficulty in demolding lead to many samples being rendered unusable during this step. Various parameters were changed to generate better pressing outcomes and they are outlined in Table 5.

The extruder shown in Section 3.4 was manufactured as an improvement to the previously mentioned design. Figure 24 compares both, with Sharmin's extruder on the left. Crucial changes between the two extruders include using stainless steel to eliminate the presence metal corrosion, moving the location of heaters and thermocouples, exploring reservoir compacting procedures, and increasing the extrusion ratio.

The extrudate from the new setup displayed considerable improvement in the quality of the samples. The surface roughness, thickness uniformity, and material state were considered acceptable and the sample pressing step was eliminated. The following sections provided a more detailed analysis into how the changes in extruder design improved sample quality.

4.1.1 Increased Extrusion Ratio

The extrusion ratio is the comparison of the ceramic paste thickness in the reservoir to the die exit thickness. Analogous to ceramic extrusion, research in aluminum extrusion suggests that softer alloys require higher extrusion ratios [36]. An indication of non-sufficient extrusion ratios is tearing at the edges of the extrudate [25]. Due to these findings, an increase in the extrusion ratio was investigated.

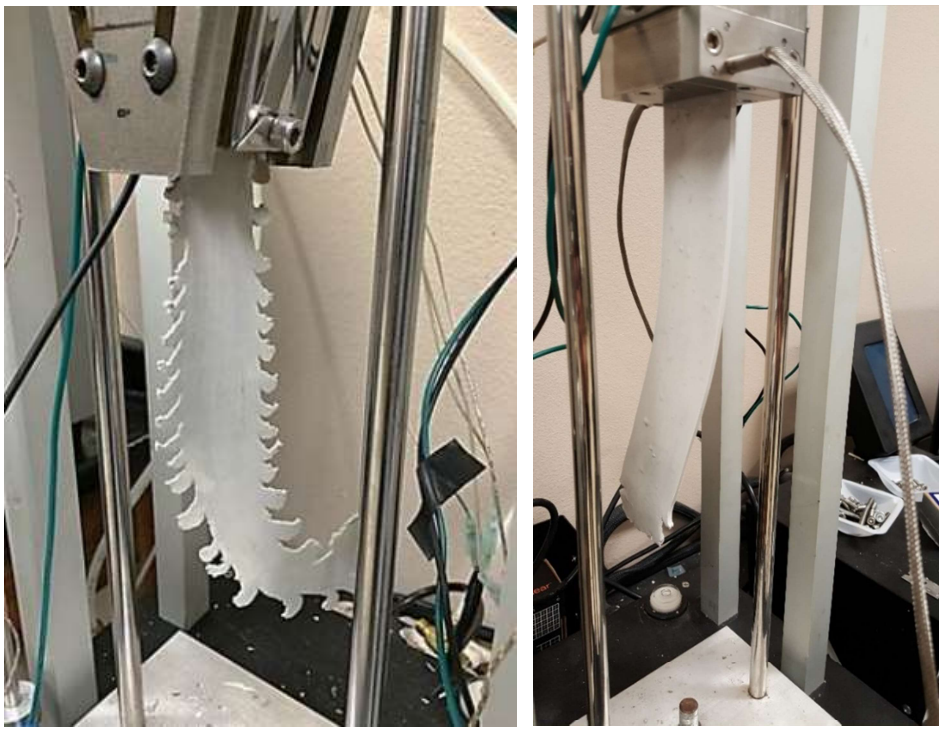

Figure 25: Decrease in edge tearing due to a higher extrusion ratio. Previous extruder (left) [13] with an extrusion ratio of 2 and the new design (right) with an extrusion ratio of 6.

Figure 25 illustrates the effect of an increase in the extrusion ratio. The image on the left shows the previously used extruder which has an extrusion ratio of 2 when outputting a target of 3.5 mm thick samples. As shown, large distortions were found on the edges of the extrudate giving reason to believe that the extrusion ratio is too small.

An increase in the extrusion ratio will also increase the extrusion velocity in the die at comparable piston speeds. This introduces higher shear rates on the sample surface. As mentioned in Section 2.3, higher shear rates can result in surface deformations called sharkskin. However, the extrudate did not exhibit these traits, but this should be considered for further increases in extrusion ratio.

4.1.2 Sample Surface Roughness

The surface quality of a ceramic sample has a great impact on the quality of embossed microstructures. Some parameters that affect sample roughness include temperature control,

extrusion ratio, and integration of ceramic agglomerates in the reservoir. Sharmin recorded that the average roughness values for the tapes extruded with the previous extruder were ± 5 μm [13]. The information in this section will expose how changes in the design mentioned above improve the average roughness of post-extrusion samples.

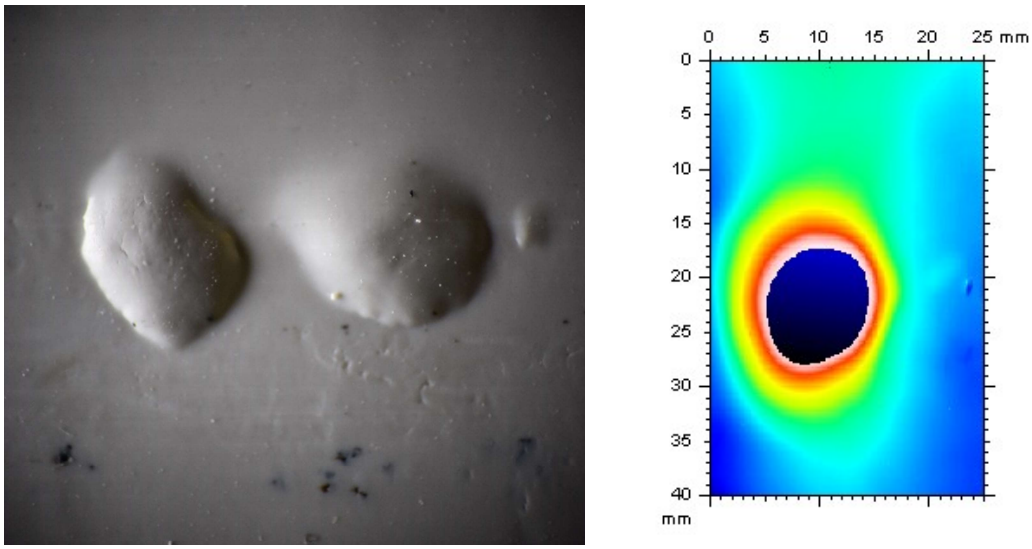

Figure 26: RTI image (left) and Optical Profile (right) of an internal air pocket.

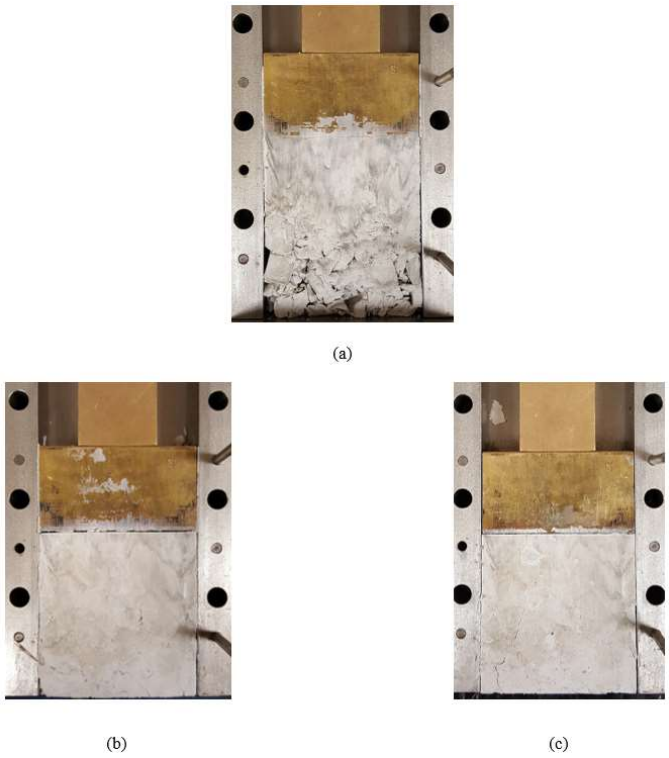

Figure 27: Ceramic feedstock after (a) 2.32 MPa, (b) 4.65 MPa, and (c) 6.97 MPa of compacting pressure.

Once temperature control and the extrusion ratio were improved, a new defect formed impacting the surface roughness. The introduction of air pockets inside the samples were observed, shown in Figure 26 and is mentioned in Section 2.2. This defect was eliminated by investigating the pre-packing procedure explained in Section 3.4. The ceramic agglomerates were loaded into the reservoir and compacted at three different pressures. Once compacted, the extruder was disassembled and the ceramic feedstock was inspected. It was found that a pressure of 6.97 MPa was sufficient to fully incorporate the material into a single component, shown in Figure 27. This is compared to a 5.62 MPa compacting pressure used in the previous design.

Optical Profilometer results show that samples from the new extruder exhibit much lower surface roughness. Smaller sections of the samples were analyzed for flatness. Areas the same size as the embossed microfluidic testing area showed an average surface roughness of

$\pm$ 2.03 µm. This is compared to an average surface roughness of $\pm$ 5 µm reported by Sharmin [13].

4.2 Embossing

The embossing process involves pressing a ceramic sample on to the Nickle embossing plate shown in Figure 20. Figure 28 gives the optical scan profile of the test section for the embossing plate, and the experimental method is also shown in Section 3.6.

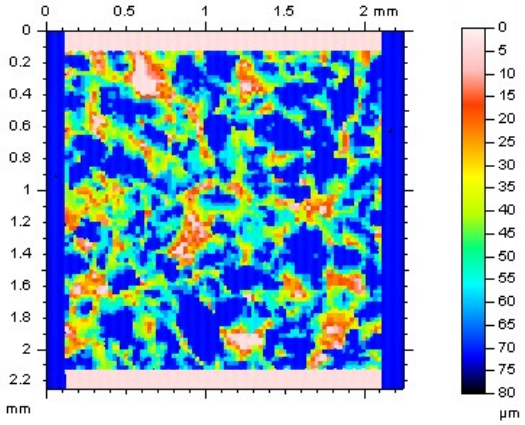

Figure 28: Optical scan of the embossing plate used for this study.

Condition of embossed microstructures depends on the average particle size of the precursor powder, the surface quality of pre-embossed samples, viscosity of the ceramic, and speed of embossing. The last section described the process of improving the surface quality of pre-embossed samples and this following section will describe how varying the other parameters affected the embossed samples. The quality of post-embossed samples was judged on the definition of the edges around the testing region, resolution of the embossed microstructures compared to the embossing plate, and the amount of material left on the embossing plate. Table 6 shows a list of iterations tried and the outcomes observed.

Table 6: List of embossing conditions varied and the subsequent response.

Embossing						
Iteration	**MFI (g/10min)**	**Extruder Used**	**Pre-heat Embossing Components? / Release Agent Used**	**Embossing Time / Temperature**	**Cooling Environment**	**Observation**
1	19	Sharmin	No/Stoner©	2.29s/120˚C	Ambient	Difficult demolding and loss of material on embossing plate, microstructures not well defined
2	19	Sharmin	No/Mold Wiz©	2.29s/120˚C	Ambient	Easier demolding but material still left on plate, microstructures not well defined
3	57	Sharmin	No/Mold Wiz©	2.29s/120˚C	Ambient	Very easy demolding and little material left on plate, poorly defined microstructures
4	19	Robbins	No/Mold Wiz©	2.29s/120˚C	Ambient	Difficult demolding with lots of material left on plate, well defined microstructures
5	57	Robbins	No/Mold Wiz©	2.29s/120˚C	Ambient	Easy demolding and little loss of material on plates, microstructures are less defined than with low MFI
6	19	Robbins	Yes/Mold Wiz©	2.29s/120˚C	Ambient	Difficult demolding and some material left on embossing plate, microstructures well defined, cracks form in test section
7	57	Robbins	Yes/Mold Wiz©	2.29s/120˚C	Ambient	Easy demolding and little loss of material on plates, improved microstructures but still less defined than with low MFI, small cracks form in test section
8	57	Robbins	Yes/Mold Wiz©	2.29s/120˚C	On Refrigerated Surface	No change from ambient results
9	57	Robbins	Yes/Mold Wiz©	2.29s/120˚C	In Press	Very difficult to demold and lots of material left on plates, samples rendered unusable
10	57	Robbins	Yes/Mold Wiz©	2.29s/110˚C	Ambient	More difficulty demolding than 120˚C embossing and loss in microstructure quality, cracks became larger
11	57	Robbins	Yes/Mold Wiz©	9.91s/120˚C	Ambient	Easy demolding with a minimal amount of material left on plates, microstructures very well defined and extent of post-embossing cracks reduced.

4.2.1 Varying Melt Flow Index of Thermoplastic Binder

Figure 29 and 30 compare optical scan of two different MFIs of the thermoplastic binder (EVA). From these results the low melt flow, high viscosity, binder provided more well-defined edges but demonstrated difficulties during demolding from the embossing plate. Difficulty in demolding is attributed to the low elasticity of the high viscosity polymer. For this reason, high MFI material was used for the remainder of the study.

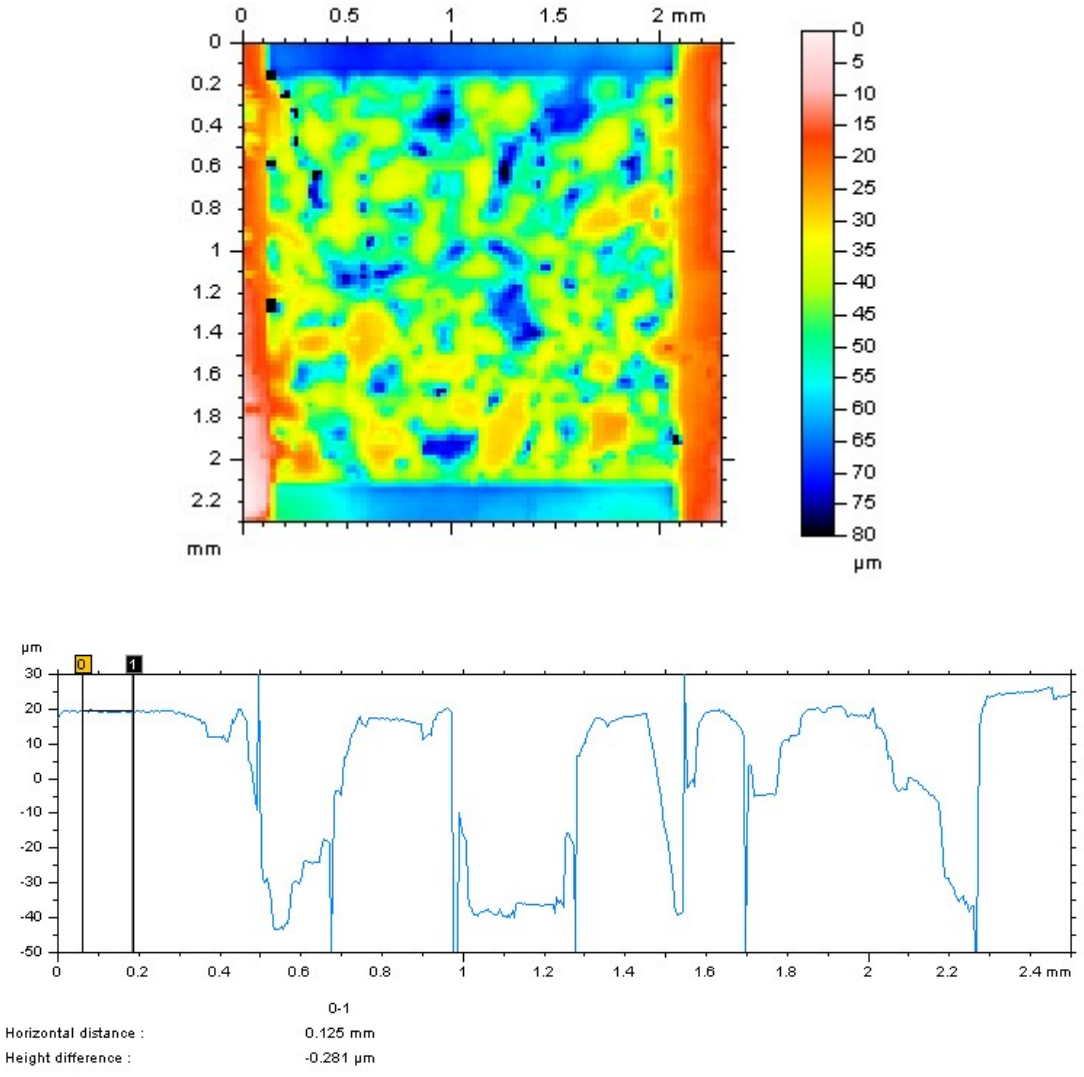

Figure 29: Optical scan of post-embossing low MFI (19g/10min). Embossed at 120˚C.

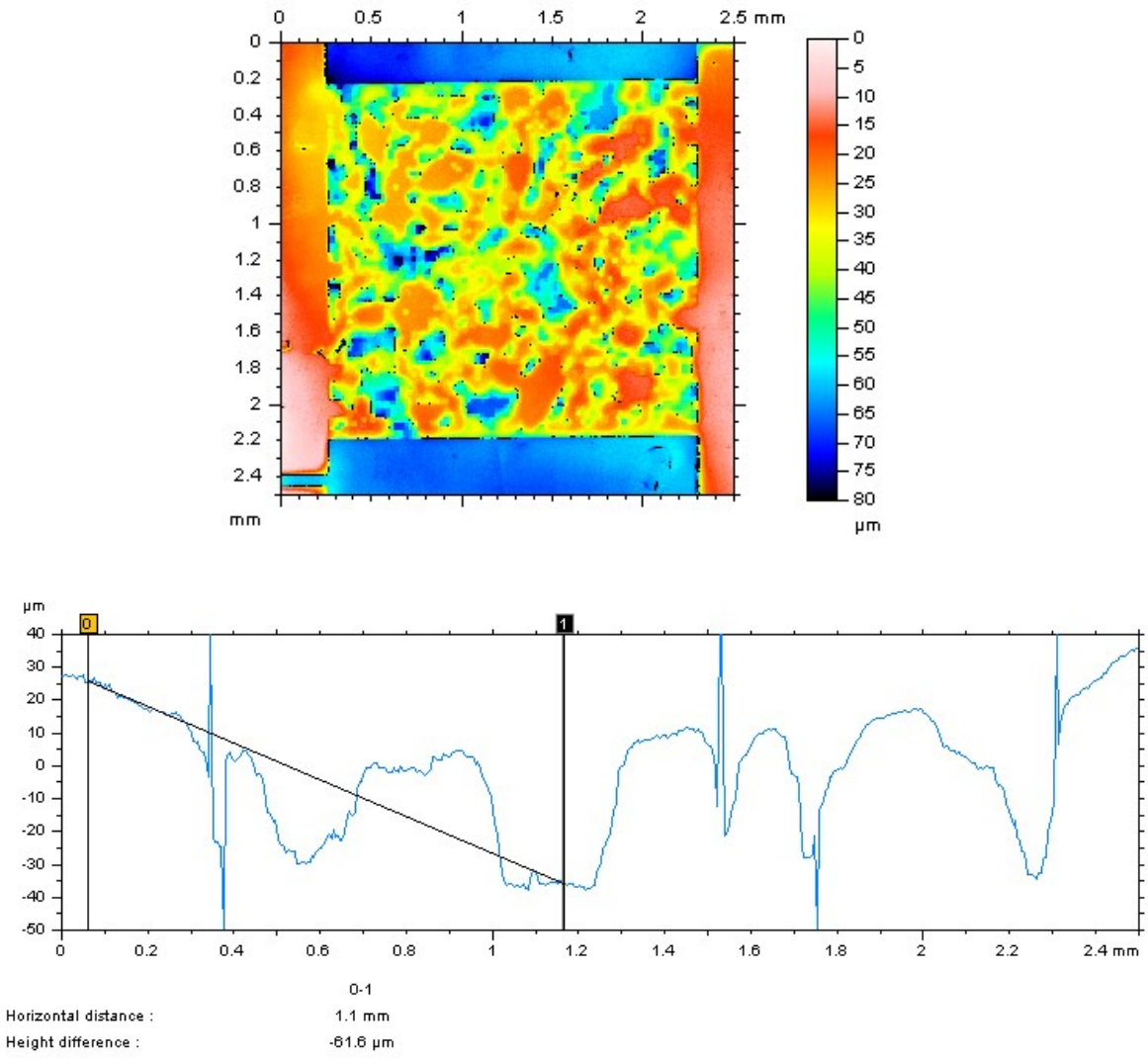

Figure 30: Optical scan of post-embossing high MFI (57g/10min). Embossed at 120˚C.

4.2.2 Embossing Speed

During embossing, the Carver © hydraulic press was allowed to reach a pressing force of 1.25 metric tons before relieved. The samples were embossed at 2 different speeds, $2.29 \pm .39$ s and $9.91 \pm .90$ s. Due to the pressing being manually driven, more accurate embossing speeds could not be obtained. It was recorded that the slower embossing speed resulted in even higher resolution microstructures and flattened the edges around the testing section. Due to lower speed,

the material was able to adequately fill the voids of the embossing plate by allowing more time to react to the displaced volume. Figure 31 shows the resulting microstructure optical scan.

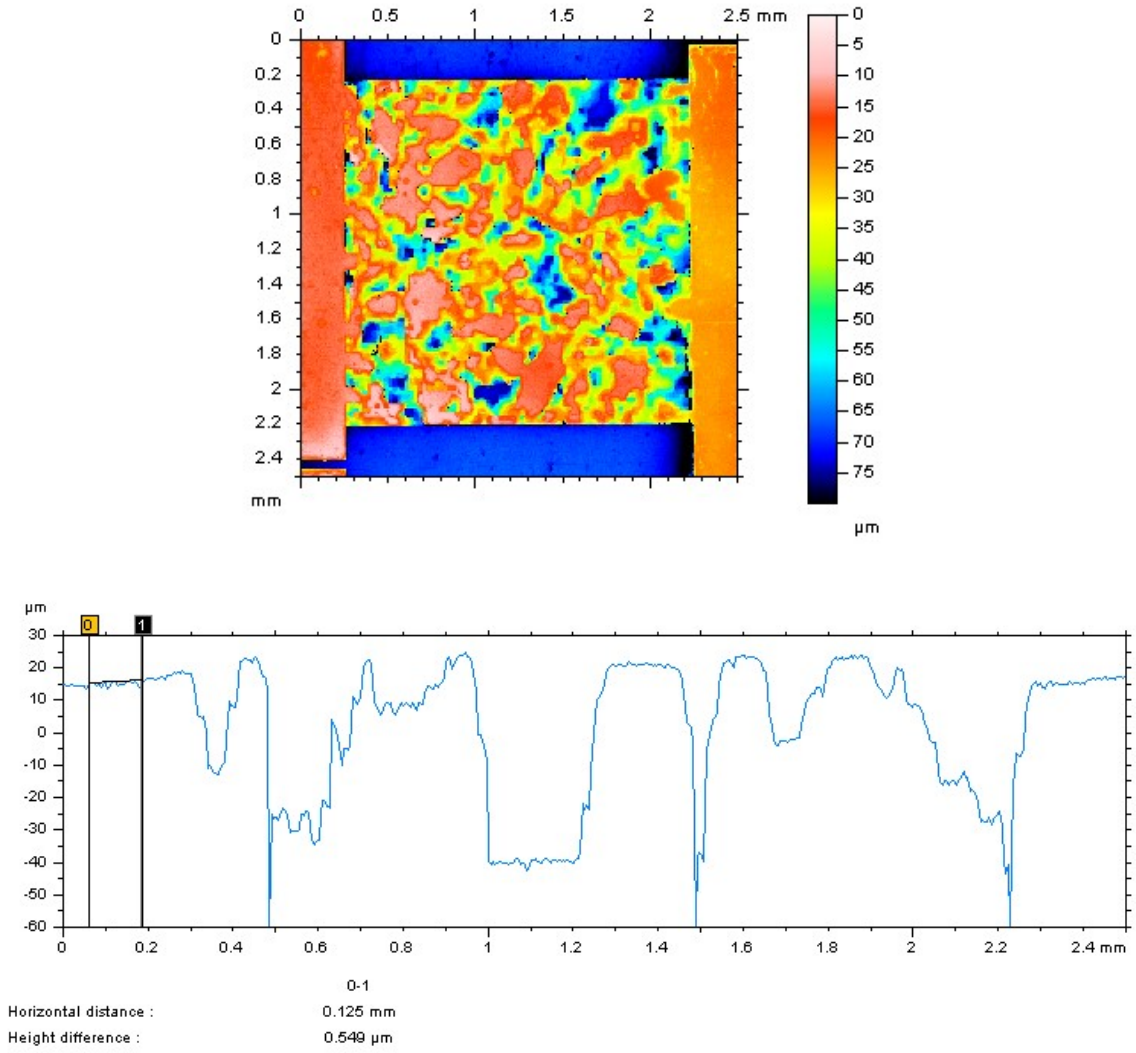

Figure 31: Slowly pressing the material onto the embossing plate resulted in higher resolution microstructures.

4.2.3 Post-Embossed Cracking Mitigation

Once high-resolution microstructures were achieved, cracks began to form in the samples. This was attributed to high stress concentrations in high displacement areas. Several steps were

taken to mitigate observed cracks such as changing the embossing temperature, rate of cooling before demolding, and the introduction of an annealing step.

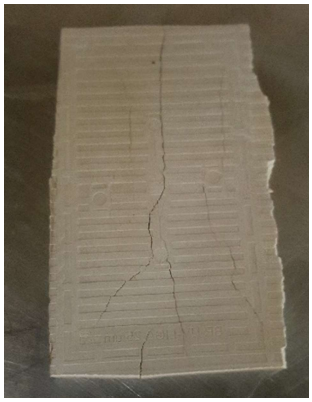

(a)

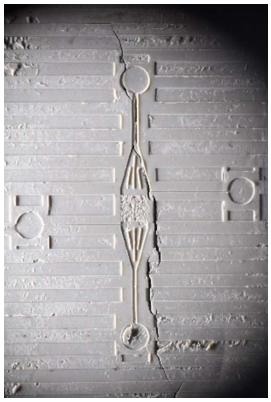

(b)

(c)

Figure 32: Post-embossing cracks after (a) 12 hours holding time at 120°C after demolding, (b) annealing though slow cooling after demolding, and (c) slow cooling of non-demolded sample.

Samples left in the oven at the embossing temperature were discolored and became brittle. This can be seen in Figure 32(a). The best results were found using a slow cooling method after the sample had been demolded as shown in Figure 32(b). The samples were cooled inside of an oven that was set to 120°C and then turned off after placing the sample inside. This allowed time for the internal stresses of the ceramic to dissipate reducing crack size and depth. When samples

were not removed from the embossing plate prior to cooling, demolding of the ceramic left increased amounts of material on the embossing plate as internal stresses were not able to be relieved. Figure 32(c) illustrates these results. Overall the cracks have been reduced but not removed.

4.2.4 Optimal Alumina Ceramic Manufacturing Parameters

Several parameters were varied in an effort to achieve the optimal microfluidic testing component. This includes the ceramic formulation used to obtain properly sintered samples, exploring the impacts of extrusion ratio on sample quality, varying embossing parameters as mentioned above, and investigating the capping process.

The process used to achieve this goal starts at batching the material at a 55% solid loading of Alumina [13]. This is done to ensure complete solid state sintering [13]. Once batched, the ceramic agglomerates were processed to the desired shape using a ram extruder. It was concluded that the higher extrusion ratio produced less surface and edge distortions due to higher bonding of powder molecules in the polymer matrix. This is explained in Section 2.4.
After the desired geometry and quality extrudate was obtained, hot embossing was the next step. Table 6 outlines the iterations used to investigate the hot embossing process. The optimal samples were obtained through slowly embossing the ceramic samples that were batched using a low viscosity polymer. Both of these parameters play an important role in filling the voids of the embossing plate shown in Figure 20. The low viscosity polymer enables the ceramic material to completely flow into the cavities while slowly embossing the ceramic gives time for the surrounding material to react during pressing.

As the resolution of embossing increased, cracks began to form in high displacement areas, Figure 32. The crack mitigation technique that displayed the best results was when the sample,

removed from the embossing plate, was slowly cooled in a pre-heated (120˚C) oven. Residual stresses after embossing were allowed to dissipate using this method but cracks were not yet completely removed.

Once embossed, post-processing heat treatments were used to create fully vitrified samples. A two-step debinding process was used to remove the PEG and EVA. By first removing the water soluble binder, adequate pore space was provided for the gaseous decomposition of the thermoplastic binder [13]. Sintering of the ceramic was carried out by the heating schedule outlined in the appendix.

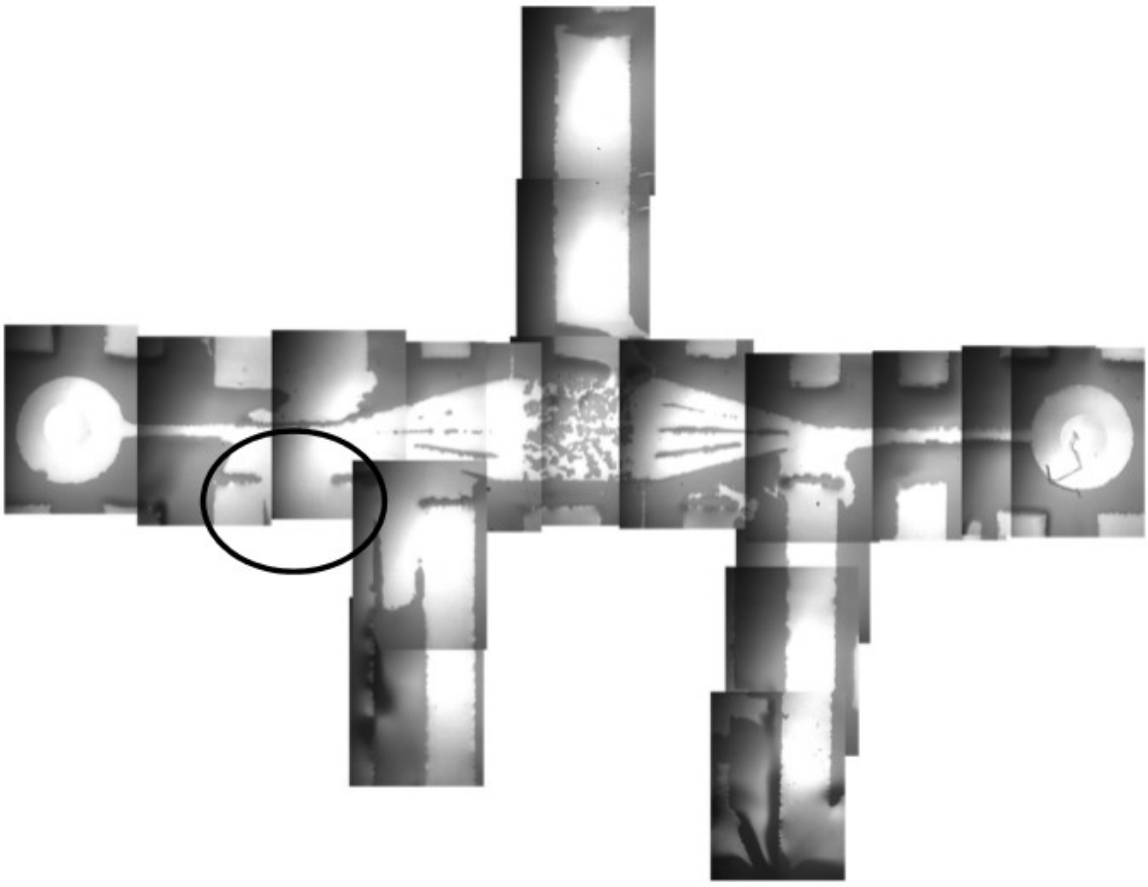

Figure 33: Capping of Alumina ceramics.

Finally, capping of the material was accomplished by heating a borosilicate microscope slide to its softening temperature (720˚C) on top of a sintered ceramic sample. Incomplete capping

was observed however. Attempts at further increasing the temperature, 750-800˚C, were made but resulted in less adhesion to the samples. Figure 33 shows the capping results of a sample capped at 720˚C.

4.3 Berea Sandstone Ceramics

The final objective of this study was to manufacture a ceramic microfluidic chip made from ground Berea sandstone. By matching the permeability, porosity, and chemical composition of the real rock, a more comprehensive study of its microfluidic flow behavior can be achieved. The average particle size was 1 μm and is shown in Figure 33. The formulation of the Berea sandstone ceramic paste can be found in Section 3.1.

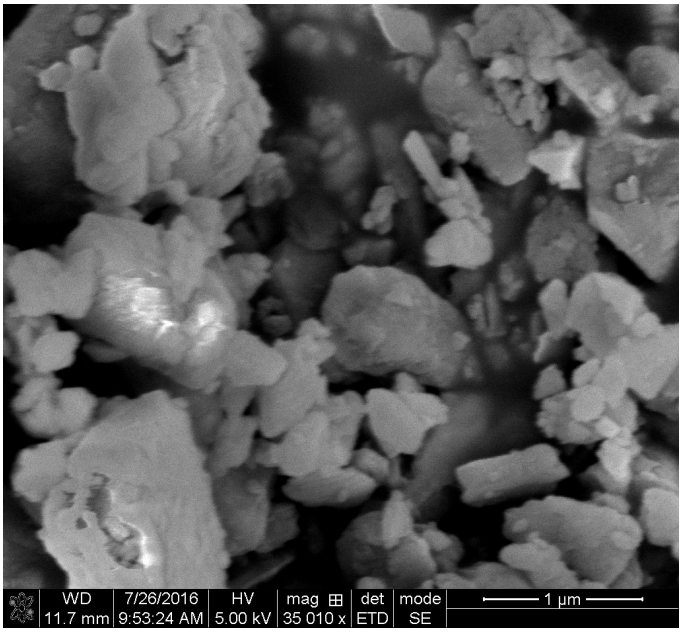

Figure 34: SEM scan of the ground Berea sandstone.

4.3.1 Embossing

After success with embossing of alumina ceramics, sintering of Berea sandstone based ceramics were studied. High melt flow EVA was used to create the paste due to its high viscosity

and ease of demolding. However, the increased particle size of the Berea ceramic resulted in lower quality microstructures shown in Figure 34.

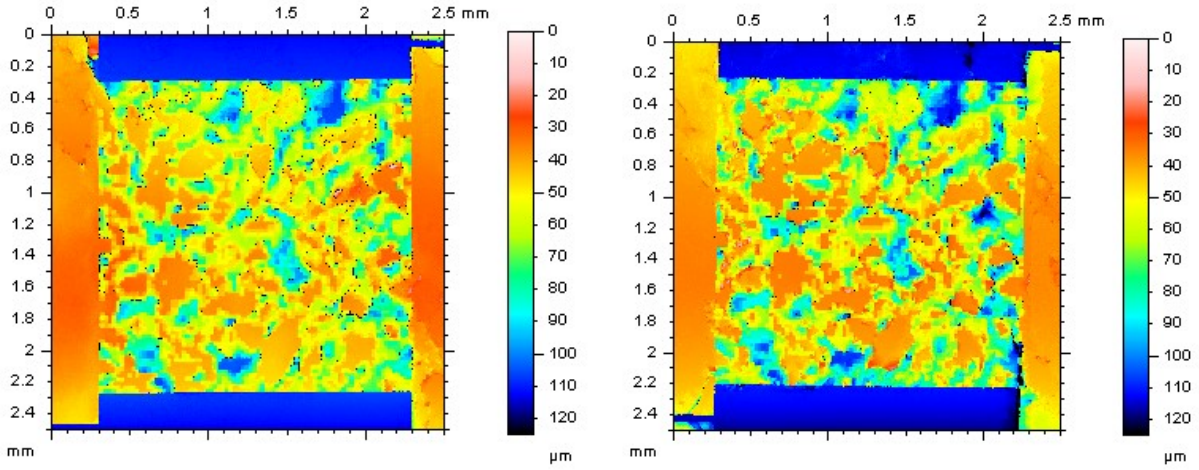

Figure 35: Optical scan of the embossed surface features on Berea sandstone samples.

4.3.2 Sintering

A preliminary study into the sintering of Berea sandstone ceramics was conducted. Sintering was attempted at 3 different temperatures: 1232˚C, 1336˚C, and 1450˚C. The heating schedule can be found in the Appendix. The first 2 temperatures were chosen because they are within the sintering range for Quartz, the main constituent in Berea sandstone.

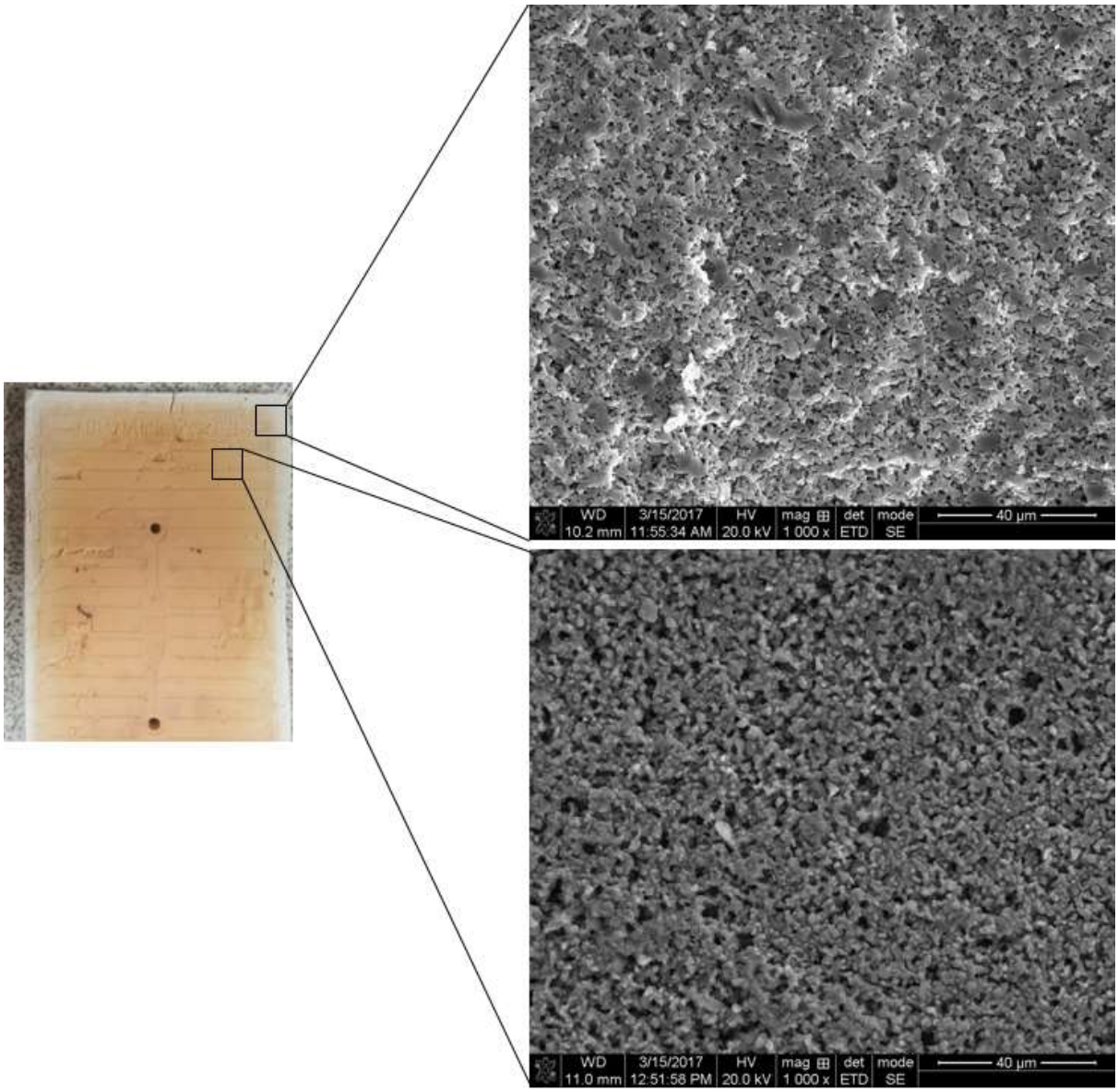

Figure 36: SEM analysis to see if sintering had occurred at 1336˚C. Images show that the periphery of the samples exhibited higher amounts of densification than the center.

Table 7: EDAX analysis comparing the chemical composition between the edge and central portions of a post-sintered Berea ceramic.

Element	Center of Sample (%wt.)	Edge of Sample (%wt.)
Carbon	1.86	1.7
Oxygen	53.04	52.91
Aluminum	0.77	0.88
Silicon	43.84	44.13
Iron	0.5	0.38

Figure 37: Sintering at 1450˚C resulted in warping and cracking of the Berea sample.

Figure 35 shows the post-sintered sample. A higher degree of densification occurred on the periphery of the sample where a loss of the reddish color in the sandstone was observed. Table 7 below shows that a loss of iron oxide on the outsides of the sample was taking place. During sintering the sample is placed on a bed of alumina pellets, a hypothesis is that the iron oxide is diffusing into the alumina due to the high temperatures.

The last temperature, 1450˚C, was chosen to see if higher temperatures would induce sintering further. As shown in Figure 36, major cracking was found throughout the sample. This was attributed to the formation of β-quartz crystalline phases. A 2Θ scan should now be performed to validate this hypothesis.

Chapter 5
Conclusions and Future Work

5.1 Conclusion

The objective of this study is providing a cost efficient way to produce microfluidic ceramic chips for analysis of fluid flow through natural rock, mainly Berea Sandstone. Prior to the study using sandstone however, a comprehensive study on hot embossing alumina ceramics was conducted. This was achieved through the combination of a thermoplastic polymer binder (Poly-ethylene-vinyl acetate), a water-soluble binder (Poly-ethylene-glycol), and the precursor powder. The combination of these into a ceramic paste is then extruded, hot embossed, sent through a two-step debinding process, and then sintered to create the micro-fluidic chips used for fluid flow analysis.

First, a redesign of the ram extruder was used to study the effects of temperature uniformity and extrusion ratio on the quality of post-extrusion ceramic samples. After revising the compacting procedure of the ceramic paste before extrusion, considerable improvement on sample surface quality was observed. Embossing of alumina ceramics was then studied by changing the MFI of the thermoplastic binder, varying the embossing temperatures, and changing the embossing speed. The best results came from using high MFI ceramic pastes and subjecting those to slower embossing speeds. This produced the highest quality microstructures and lowest amount of post-embossing surface distortions.

The quality and repeatability of embossed surface features on alumina ceramics allows the project to move into its next phase, manufacturing of a Berea sandstone microfluidic chip. Preliminary results show that sintering and resolution of embossed structures will be a challenge. Below are recommendations for the next phase of the study.

5.2 Future Work

In order to achieve higher resolution when embossing Berea ceramics, the average particle size of the sandstone precursor powder should be decreased to around the same size as the alumina powder. Right now, the average particle size is 1 μm for Berea sandstone and .15 μm for alumina. A lower particle size will not only help in the batching process but also allow for proper filling of the embossing plate during compression.

The author recommends exploring a fast firing technique such as those used the porcelain stoneware sintering for the densification of Berea sandstone. Section 2.5 explains that prolonged holding times and high sintering temperatures reduce the strength of silica/quartz ceramics and well as increases the pore sizes through the expulsion of trapped gases. The formation of β-quartz is also another culprit that could be leading to poorly densified samples. Therefore exploring sintering under a vacuum or in an inert, Helium or Argon, atmosphere should also be considered.

If complete densification is not achieved or if vitrification of quartz leads to loss of material properties, another approach recommended is to seal a Berea sandstone samples on all surfaces. The sample can be sealed with an epoxy on the non-test sections and glass used to cap the microstructures to allow for optical analysis. After the sample has become completely saturated, flow across the microchannels should be observed and analyzed.

Another recommendation is to have new extruder dies created to test the further increase of the extrusion ratio. By working the material more, a stronger interlocking of the material should help to reduce surface cracks after embossing. Reinstating the sample pressing step prior to embossing may also reduce cracks in the post-embossed sample as well.

In order to further reduce cracks, promise has been shown in the annealing step used to reduce the post-embossed ceramic's internal stresses. It is recommended to investigate this further by cooling sample more slowly or holding the sample at a lower temperature for a prolonged period.

Incomplete capping of the ceramic samples was observed for all temperatures from 720-800˚C. The author recommends investigating longer holding times at 720˚C, the glass softening point.

Finally, a new embossing plate should be fabricated which rounds the sharp edges of the testing channel. The sharp edges create places of high residual stresses which can result in cracking around the testing area.

Bibliography

[1] V. A. Lifton, "Microfluidics: an enabling screening technology," *National Center for Biotechnology Information,* vol. 10, no. 16, pp. 1777-1796, 2016.

[2] G. M. Whitesides, "The orgins and the future of microfluidics," *Nature,* vol. 442, no. 7101, pp. 368-373, 2006.

[3] K. F. Jensen, "DSpace@MIT," 2003. [Online]. Available: http://hdl.handle.net/1721.1/7995. [Accessed 23 March 2017].

[4] United States Environmental Protection Agency, "Carbon Dioxide Capture and Sequestration," United States Environmental Protection Agency, 9 August 2016. [Online]. Available: https://www3.epa.gov/climatechange/ccs/. [Accessed 23 March 2017].

[5] C. S. Effenhauser, A. Paulus, A. Mans and H. M. Widmer, "High-Speed Separation of Antisense Oligonucleotides on a Micromachined Capillary Electrophoresis Device," *Analytical Chemistry,* vol. 18, no. 66, pp. 2949-2953, 1994.

[6] A. T. Woolley and R. A. Mathies, "Ultra-High-Speed DNA Sequencing Using Capillary Electrophoresis Chips," *Analytical Chemistry,* vol. 20, no. 67, pp. 3676-3680, 1995.

[7] A. Muggeridge, A. Cockin, K. Webb, H. Frampton, I. Collins, T. Moulds and P. Salino, "Recovery rates, enhanced oil recovery and technological limits," *Philosophical Transactions of the Royal Society A,* vol. 2006, no. 372, p. 20120320, 2013.

[8] P.-E. Oren and S. Bakke, "Reconstruction of Berea sandstone and pore-scale," *Journal of Petroleum Science and Engineering,* Vols. 3-4, no. 39, pp. 177-199, 2003.

[9] J. Hanania, K. Stenhouse and J. Donev, "Oil and Gas Traps," Energy Education, [Online]. Available: http://energyeducation.ca/encyclopedia/Oil_and_gas_traps. [Accessed 25 June 2017].

[10] J. Caldwell, A. Chowdhury, P. van Bemmel, F. Engelmark, L. Sonneland and N. S. Neidell, "Schlumberger," 1997. [Online]. Available: https://www.slb.com/~/media/Files/resources/oilfield_review/ors97/win97/traps.pdf. [Accessed 25 June 2017].

[11] U.S. Energy Information Administration, "Short-Term Energy Outlook," 6 June 2017. [Online]. Available: https://www.eia.gov/outlooks/steo/pdf/steo_full.pdf. [Accessed 23 June 2017].

[12] L. Romero-Zeron, "Advances in Enhanced Oil Recovery," 2012. [Online]. Available: http://cdn.intechopen.com/pdfs/37036/InTech-Advances_in_enhanced_oil_recovery_processes.pdf. [Accessed 31 March 2017].

[13] K. Sharmin, "FABRICATION AND CHARACTERIZATION OF MINIATURIZED COMPONENTS BASED ON EXTRUDED CERAMIC-FILLED POLYMER BLENDS," *LSU Doctoral Dissertations,* p. 919, 2015.

[14] M. Sahli, T. Barriere and J.-C. Gelin, "Finite element simulation and experimental investigation of hot embossing of thin polymer film," *International Journal for Simulation and Multidisciplinary Design Optimization,* vol. 4, no. 2, pp. 101-106, 2010.

[15] J.-d. Chen and J. Koplik, "Immiscible fluid displacement in small networks," *Journal of Colloid and Interface Science,* vol. 108, no. 2, pp. 304-330, 1985.

[16] B. T. Campbell and F. M. Orr Jr., "Flow Visualization for CO2/Crude-Oil Displacements," *Society of Petroleum Engineers Journal,* vol. 25, no. 5, pp. 665-678, 1985.

[17] J. Joseph, "Quantification of transport properties in microfluidic porous media," University of Alberta, 2012.

[18] J. R. Moore, S. D. Glaser, H. F. Morrison and G. M. Hoversten, "The streaming potential of liquid carbon dioxide in Berea sandstone," *Geophysical Reference Letters,* vol. 31, no. 17, 2004.

[19] L. D. Thanh and R. Sprik, "Zeta Potential Measurement Using Streaming Potential in Porous Media," *Journal of Science: Mathematics - Physics,* vol. 31, no. 4, pp. 56-65, 2015.

[20] S. Devasenathipathy and J. Santiago, Electrokinetic flow diagnostics. In: Breuer KS (ed), Micro- and nano-scale diagnostic techniques, Springer: New York Berlin Heidelberg (in press), 2004.

[21] R. J. Hunter, Zeta Potential in Colloidal Science, San Diego: Acedemic P XI, 1988.

[22] S. Trinh, P. Arce and B. R. Locke, "Effective Diffusivities of Point-Like Molecules in Isotropic Porous Media by Monte Carlo Simulation," *Transport in Porous Media,* vol. 38, no. 3, pp. 241-259, 2000.

[23] P. Vielma-Thomas, A. Cervera, B. Levenfeld and A. Varez, "Production of alumina parts by powder injection molding with a binder system based on high density polyethylene," *European Ceramic Society,* vol. 28, no. 4, pp. 763-771, 2007.

[24] X. Yang, C. Jia, Z. Xie, W. Liu and Q. Liu, "Water-Soluble Binder System Based on Poly-Methyl Methacrylate and Poly-Ethylene Glycol for Injection Molding of Large-Sized Ceramic Parts," *Applied Cermaic Technology,* vol. 10, no. 2, pp. 339-347, 2012.

[25] V. Hristov, E. Takacs and J. Vlachopoulos, "Surface tearing and wall slip phenomena in extrusion of highly filled HDPE/wood flour composites," *Polymer Engineering and Science,* vol. 46, no. 9, pp. 1204-1214, 2006.

[26] M. S. Mason, T. Huang, R. G. Landers, M. C. Leu and G. E. Hilmas, "Aqueous-based extrusion of high solids loading ceramic pastes: Process modeling and control," *Journal of Materials Processing Technology,* pp. 2946-2957, 2009.

[27] F. N. Cogswell, "Converging Flow of Polymer Melts in Extrusion Dies," *Polymer Engineering and Science,* vol. 12, no. 1, 2004.

[28] B. V. Mehta, S.-H. Chen, I. Al-Zkeri, Gunasekera and A. Buijk, "A step towards the design of feeder plates for extrusion dies," in *Simulation of Material Processing: Theory, Methods and Applications*, Tokyo, A. A. Balkema Publishers, 2001, pp. 455-460.

[29] J. Vlachopoulos and D. Strutt, "The Role of Rheology in Polymer Extrusion," [Online]. Available: http://www.polydynamics.com/Rheology.pdf. [Accessed 17 3 2017].

[30] E. Muliawan, S. Hatzikiriakos and M. Sentmanat, "Melt fracture of linear PE," *International Polymer Processing,* vol. 20, no. 1, pp. 60-67, 2005.

[31] Y. Mahmoodkhani, *Mathematical Modelling of the Material Flow and Microstructural Evolution During the Extrusion of AA3003 Aluminum Alloy,* Waterloo: University of Waterloo, 2013.

[32] M. S. Mason, T. Huang, R. G. Landers, M. C. Leu and G. E. Hilmas, "Freeform Extrusion of High Solids Loading Ceramic Slurries, Part I: Extrusion Process Modeling," University of Missouri, Rolla, 2006.

[33] E. Miller and J. P. Rothstein, "Control of Sharkskin instability in the extrusion of Polymer Melts Using Induced Temperature Gradients," *Rheologica Acta,* vol. 44, no. 2, pp. 160-173, 2004.

[34] H. H. Winter and E. Fischer, "Processing History in Extrusion Dies and its Influence on the State of the Polymer Extrudate at the Die Exit," *Polymer Engineering and Science,* vol. 21, no. 6, pp. 366-374, 1981.

[35] J. Zhou, T. Druzdzel and J. Duszczyk, "The effect of extrusion parameters on the fretting wear resistance of Al-based composites produced via powder metallurgy," *Journal of Material Science,* vol. 34, pp. 5089-5097, 1999.

[36] Bonnell Aluminum, "Aluminum Extrusion Process," Bonnell Aluminum, [Online]. Available: https://www.bonlalum.com/education/aluminum_extrusion_process.shtml. [Accessed 14 June 2017].

[37] Berea Sandstone Landscaping Products, "Berea Sandstone Petroleum Cores," Berea Sandstone Landscaping Products, [Online]. Available: http://www.bereasandstonecores.com/cores.php. [Accessed 16 December 2016].

[38] Certified Porcelain Tile, "ptcaonline," The Porcelain Tile Certification Agency, [Online]. Available: http://www.ptcaonline.org/. [Accessed 4 July 2017].

[39] J. Martin-Marquez, J. M. Rincon and M. Romero, "Effect of firing temperature on sintering of porcelain stoneware tiles," *Ceramics International,* vol. 34, no. 8, pp. 1867-1873, 2008.

[40] C. Zanelli, M. Raimondo, M. Dondi, G. Guarini and P. Tenorio Cavalcante, "Sintering Mechanisms of Pocelain Stoneware Tiles," in *7th World Congress on Ceramic Tile Quality*, Castellón, 2004.

[41] C. Zanelli, M. Raimondo, G. Guarini and M. Dondi, "The vitreous phase of porcelain stoneware: Composition, evolution during sintering and physical properties," *Journal of Non-Crystalline Solids,* vol. 357, no. 16-17, pp. 3251-3260, 2011.

[42] W. Lee and Y. Iqbal, "Influence of Mixing on Mullite Formation in Porcelain," *Journal of the European Ceramic Society,* vol. 21, no. 14, pp. 2583-2586, 2001.

[43] I. Johari, S. Said, B. Hisham, A. Bakar and Z. A. Ahmad, "Effect of the Change of Firing Temperature on Microstructure and Physical Properties of Clay Bricks from Beruas (Malaysia)," *Science Of Sintering,* vol. 42, pp. 245-254, 2010.

[44] J.-G. Song, F. Wang, X.-B. Bai, D.-M. Du, Y.-Y. Ju, M.-H. Xu and G.-C. Ji, "Effect of the sintering technology on the properties of fired brick from quartz sands," *Journal of Ceramic Processing Research,* vol. 12, no. 4, pp. 357-360, 2011.

[45] Y. S. Han, J. B. Li and Z. H. Wen, "The Effect of Sintering Temperature on Porous Silica Composite Strength," *Journal of Porous Material,* vol. 10, no. 1, pp. 41-45, 2003.

[46] W. Wan, C.-e. Huang and J. Z. J. Q. T. Yang, "Effect of Sintering Temperature on the Properties of Fused Silica Ceramics Prepared by Gelcasting," *Journal of Electronic Material,* vol. 43, no. 7, pp. 2566-2572, 2014.

[47] S. Reynolds, "Quartz vs. Fused Silica: What's the Difference?," Swift Glass, 8 September 2015. [Online]. Available: http://www.swiftglass.com/quartz-vs-fused-silica-whats-the-difference/. [Accessed 9 July 2017].

[48] R. Breneman and J. Halloran, "Hysteresis upon Repeated Cycling through the Beta-Alpha Cristobalite Transformation," *Journal of Ceramic Science and Technology,* vol. 6, no. 1, pp. 55-62, 2015.

[49] O. Yong-Taeg, S. Fujino and K. Morinaga, "Fabrication of transparent silica glass by powder sintering," *Science and Technology of Advanced Materials,* vol. 3, no. 4, pp. 297-302, 2002.

[50] K. Orii, Y. Hara, T. Akiyama, K. Tsukuma and Y. Kikuchi, "Process for production of pure transparent quartz". United States of America Patent US5665133 A, 9 September 1997.

[51] Sigma-Aldrich, "MSDS - 340502," 2 June 2016. [Online]. Available: http://www.sigmaaldrich.com/MSDS/MSDS/DisplayMSDSPage.do?country=US&language=en&productNumber=340502&brand=ALDRICH&PageToGoToURL=%252Fcatalog%252Fproduct%252Faldrich%252F340502%253Flang%253Den. [Accessed 5 June 2017].

[52] Sigma-Aldrich, "MSDS - 437220," 2 June 2016. [Online]. Available: http://www.sigmaaldrich.com/MSDS/MSDS/DisplayMSDSPage.do?country=US&language=en&productNumber=437220&brand=ALDRICH&PageToGoToURL=%252Fcatalog%252Fproduct%252Faldrich%252F437220%253Flang%253Den. [Accessed 5 June 2017].

[53] Cleveland Quarries, "Physical Properties of Berea Sandstone," Alt Media Studios, [Online]. Available: http://www.clevelandquarries.com/technical-data. [Accessed 23 July 2017].

[54] M. Aminzare, F. Golestani-fard, O. Guillon, M. Mazaheri and H. Rezaie, "Sintering Behavior of an Ultrafine Alumina Powered Shaped by Pressure Filtration and Dry Pressing," *Materials Science and Engineering: A,* vol. 527, no. 16-17, pp. 3807-3812, 2010.

[55] F. A. T. Guimaraes, K. L. Silva, V. Trombini, J. Pierri, J. A. T. R. Rodrigues and E. M. J. A. Pallone, "Correlation between microstructure and mechanical properties of Al2O3/ZrO2 nanocomposites," *Ceramics International,* vol. 35, no. 2, pp. 741-745, 2009.

[56] "alfa= Aluminum Oxide," Inframat Advanced Materials, [Online]. Available: http://www.advancedmaterials.us/26N-0802A.htm. [Accessed 5 June 2017].

[57] J. F. Pepper, W. J. De Witt and D. F. Demarest, "Geology of the Bedford Shale and Berea Sandstone in the Appalachian Basin," United States Government Printing Office, Washington D.C., 1954.

[58] Ohio EPA, "Major Aquifers in Ohio and Associated Water Quality," April 2014. [Online]. Available: http://epa.ohio.gov/Portals/28/documents/gwqcp/Aquifer&Geochem_ts.pdf. [Accessed 14 February 2017].

[59] E. Manger, "Porosity and Bulk Density of Sedimentary Rocks," United States Government Printing Office, Washington D.C., 1963.

[60] Alfa Aesar, "J19972 Polyethylene Glycol 6000, flakes, Ultrapure, Affymetrix/USB," [Online]. Available: https://www.alfa.com/en/catalog/J19972/. [Accessed 5 June 2017].

[61] avantor, "Polyethylene Glycol 200, Liquid, BAKER," J.T. Baker, [Online]. Available: https://www.avantorinc.com/commerce/product.aspx?id=2147510408. [Accessed 5 June 2017].

[62] R. Raman, W. Slike III and R. German, "Experimental Evaluation of the Mixing Process for the Preparation of Feedstock for Powder Injection Molding," *Ceram. Eng. Sci. Proc.,* vol. 14, no. 11-12, pp. 166-186, 1993.

[63] X. Xu and G. E. Hilmas, "The rheological behavior of ceramic/polymer mixtures for coextrusion processing," *Journal of Materials Science,* vol. 42, no. 4, pp. 1381-1387, 2007.

[64] Carver Inc., "Laboratory Press Leaders," Carver Inc., [Online]. Available: http://www.carverpress.com/products/benchtop-manual/heated. [Accessed 5 June 2017].

[65] AXEL Plastics Research Laboratories, "Mold Wiz F-57NC," [Online]. Available: https://axelplastics.com/sites/default/files/TD%20F-57NC.pdf. [Accessed 5 June 2017].

[66] M. N. Rahaman, Ceramic Processing, Boca Raton: Taylor & Francis Group, LLC, 2007.

[67] Cole-Parmer, "Cole-Parmer Cover glasses, 24 x 60 mm rectangular, 0.13 to 0.17 mm thickness," [Online]. Available: https://www.coleparmer.com/i/cole-parmer-cover-glasses-24-x-60-mm-rectangular-0-13-to-0-17-mm-thickness/4851130?searchterm=48511-30. [Accessed 5 June 2017].

[68] T. Kinsman, "Shoot Super Detailed Macro Photographs with an RTI Camera Rig," [Online]. Available: http://makezine.com/projects/shoot-super-detailed-macro-photographs-with-an-rti-camera-rig/.

[69] "Reflectance Transformation Imaging (RTI)," [Online]. Available: http://culturalheritageimaging.org/Technologies/RTI/.

[70] "Viscosity, Part 2: Melt Flow Index," 15 April 2015. [Online]. Available: http://www.beaumontinc.com/viscosity-part-2-melt-flow-index/.

[71] Strutt, "The Role of Rheology in Polymer Extrusion," Polydynamics, Inc., Hamilton.

[72] M. N. Rahaman, Sintering of Ceramics, Boca Raton: Taylor & Francis Group, LLC, 2008.

[73] Z. Peng and T. Sheppard, "A study on material flow in isothermal extrusion by FEM simulation," *Modelling and Simulation in Materials Science and Engineering,* vol. 12, no. 5, pp. 745-763, 2004.

[74] A. Cosentino, "Macro Photography for Reflective Transformation Imaging: A Practical Guide to the Highlights Method," *e-conservation Journal,* pp. 70-85, 2013.

[75] M. Hinson, "Cultural Heritage Imaging," 2015. [Online]. Available: http://culturalheritageimaging.org/What_We_Do/Projects/elmorro/index.html. [Accessed 25 5 2017].

[76] F. Omar, "Hot Embossing Proces sParameters: Simulation and Experimental Studies," Cardiff University, Cardiff, 2013.

[77] M. Mennig, P. W. Oliveira and H. Schmidt, "Embossing," in *Sol-Gel Technologies for Glass Producers and Users*, New York, Springer Science+Buisness Media, 2004, pp. 109-116.

Chapter 6
Appendix

6.1 Ceramic Sample Manufacturing Instructions

1. Batching
    i. Measure out the material to be used
    ii. Turn on the fuse box and compressor
    iii. Go to setup-identify-[experiment name]
    iv. Hit 'esc' to go to previous menu
    v. Go to Calibration
    vi. Enter calibration, "M" for mixing (15-20 sec.)
    vii. Enable motor-press 'ENTER'
    viii. Hit the reset button on the Rheometer
    ix. Set temperature-all will be the same enter "Y" for yes and set to 90˚
    x. Set rotor speed to 30 rpm
    xi. Hit "ENTER"
    xii. Under display-type 1,5,6 as the values
    xiii. Start at 60˚
    xiv. Hit "RUN"
    xv. Go to Graphic menu
    xvi. Press green button to start
    xvii. Pour in the material slowly and allow it to become well incorporated before adding more
    xviii. If the mixture is running too dry (material is coming back out of the top) then add drops of the liquid PEG until the material has subsided
    xix. Once all of the material is combined, allow it to mix for 10 minutes
    xx. Remove the material and allow the system temperature to stabilize
    xxi. Add the material back and let it mix for 10 more minutes to ensure proper mixing
2. Extrusion Process
    a. Pressing
        i. Hook up the C1 and C2 wires to the heating controller in series (same outlet)
        ii. Hook up the two power strips to the controller in series as well
        iii. Set thermocouple on the front plate of the extruder and one on the top of one of the brass slides (use high temperature tape)
        iv. Turn on the power strip for the controller and set to 120˚C
        v. Cut the material to be extruded onto small pieces
        vi. Place the material into the extrusion chamber
        vii. Secure the piston to the top compression plate
        viii. Allow the extruder to reach the 120˚C mark
        ix. Set the tensile tester to a speed of 1"/min and press down 1.75" (marked on the piston)
        x. Turn off the heaters, controller, and the power strips
        xi. Wait for 3 to 4 hours

b. Extrusion
    i. Open the brass slide evenly on both side to the desired thickness
    ii. Turn on the controller and set to 120˚C
    iii. Wait for the extruder to reach the desired temperature
    iv. Turn on the computer and COM-TEN tensile tester
    v. From start menu open COM-TEST
    vi. Under “configuration” select “standard compression”
    vii. Turn off auto-return
    viii. Select single test
    ix. Select save raw data and click OK
    x. Under “configuration” select “test configuration”
    xi. Set force limit to 1200 lbf, deflection to 30”, speed to .1”/min
    xii. Start test and allow the piston to travel down to the last marked place on the piston (about 2.5”)
    xiii. Watch the force gauge and make sure not to hit the brass slides
    xiv. Turn off heater and collect the extruded material
    xv. Turn off computer, tensile tester, and power strips
    xvi. Clean the extruder of all material after cool down
c. Molding
    i. Set up the temperature controller on the Carver Press
    ii. Plug in the two heaters in series
    iii. Set the temperature to 120˚C
    iv. Spray mold with a demolding agent (lightly)
    v. At 110˚C set the mold in to dry the demolding agent
    vi. Measure and record all dimensions of the ceramic chip
    vii. Use aluminum spacers to lower the thickness of the chip by .3 mm
    viii. Place the smooth side of the ceramic on the mold
    ix. Set an aluminum plate, rough surface down, on top of the ceramic
    x. Raise the press until a soft contact is made between all surfaces
    xi. Wait for 6.5 minutes
    xii. Apply a pressure of 1.25 metric tons and quickly release
    xiii. Turn off heaters and remove
    xiv. Place all components on a cold surface and allow to sit for 1 hr.
    xv. Flip over and remove the aluminum plate but leave spacers

3. Solvent Extraction
    i. Turn on oven to 45˚C (4-5 hours to reach temp.)
    ii. Record all dimensions and weight before placing in oven
    iii. Add water to glass container and to plastic weigh boats
    iv. Place sample in weigh boat
    v. Place sample in oven at 45˚C for 3-4 hr.
    vi. Take samples out and allow to dry
    vii. Record new dimensions and weight
4. Thermal De-binding
    a. Day 1
        i. Use the oven located a LSU Innovation Park
        ii. Place sample in an Alumina tray with Al_2O_3 beads in the bottom

iii. Insert the sample into the right side of the oven
iv. Use the black tape marker on push rod for correct insertion length
v. Seal the heating tube with the end caps provided
vi. Connect the N_2 cylinder to the oven and set the flow meter to 10
vii. Program the following heating schedule then start the oven

Temperature (˚C)	Time (hr)
25	3
1000	13
1000	1
25	OFF

b. Day 2
i. Turn off the N_2 cylinder
ii. Attach the Air valve to the oven and set flow meter to 10
iii. Run the oven again at the same temperature

5. Sintering
i. Use the furnace located in ERAD 128
ii. Place the sample in the Alumina tray as done in the Thermal De-binding section
iii. Plug in the furnace and place the sample inside
iv. Lock the furnace door by rotating the black switch
v. Press the top left button to cycle through and set desired temperatures and hold times
vi. Load the following heating schedule:

Temperature (˚C)	Time (min)
0	20
200	10
200	100
1000	60
1000	200
1600	60
1600	200
1000	120
400	-121

vii. Hold the down button to begin heating
viii. Allow the furnace to cool down and remove the sample

6. Capping
a. Day 1 (Bonding)
i. Use the oven located at LSU Innovation Park
ii. Load the sample into the right side of the oven
iii. Use the black tape marker on push rod for correct insertion length
iv. Program this heating schedule:

Temperature (˚C)	Time (hr:min)

25	3
720	3:51
720	1
25	off

v. Start the cycle by holding the down button

b. Day 2 (Annealing)

i. Reprogram the oven to:

Temperature (˚C)	Time (hr:min)
25	3
550	3
550	0:10
508	0:21
508	1
480	0:14
200	2:20
25	off

ii. Start the oven again

iii. Remove sample after cooled

Vita

Justin Freeman Robbins received his Bachelor's Degree from the University of Memphis in Mechanical Engineering with a second major in Physics in 2014. After taking a year off, he enrolled in the Mechanical Engineering Master's program at LSU. He worked under the guidance of Dr. Schoegl and his research is in the improvement of microstructure resolution and surface quality of extruded ceramics.

After graduation, Justin plans to move to Galveston, Texas where his wife intends to get her Bachelor's in Marine Biology. He hopes to get a job in the renewable energy field around the Houston/Galveston Area.